

## **INFORMATION TO USERS**

This manuscript has been reproduced from the microfilm master. UMI films the text directly from the original or copy submitted. Thus, some thesis and dissertation copies are in typewriter face, while others may be from any type of computer printer.

**The quality of this reproduction is dependent upon the quality of the copy submitted.** Broken or indistinct print, colored or poor quality illustrations and photographs, print bleedthrough, substandard margins, and improper alignment can adversely affect reproduction.

In the unlikely event that the author did not send UMI a complete manuscript and there are missing pages, these will be noted. Also, if unauthorized copyright material had to be removed, a note will indicate the deletion.

Oversize materials (e.g., maps, drawings, charts) are reproduced by sectioning the original, beginning at the upper left-hand corner and continuing from left to right in equal sections with small overlaps.

ProQuest Information and Learning  
300 North Zeeb Road, Ann Arbor, MI 48106-1346 USA  
800-521-0600

**UMI<sup>®</sup>**



## **NOTE TO USERS**

**This reproduction is the best copy available.**

UMI<sup>®</sup>



Models of Achernar: Evolution and Atmospheres of a rapidly rotating  
B Star

by

Catherine Lovekin

A Thesis Submitted to Saint Mary's University, Halifax, Nova Scotia in Partial Fulfillment of the  
Requirements for the Degree of

MASTER OF SCIENCE

in

Astronomy

(Department of Physics and Astronomy)

July 29, 2005, Halifax, Nova Scotia

© Catherine Lovekin, 2005

Approved: .....

Dr. R.G. Deupree  
Supervisor

Approved: .....

Dr. C.I. Short  
Examiner

Approved: .....

Dr. D. Guenther  
Examiner

Date:



Library and  
Archives Canada

Bibliothèque et  
Archives Canada

0-494-06970-8

Published Heritage  
Branch

Direction du  
Patrimoine de l'édition

395 Wellington Street  
Ottawa ON K1A 0N4  
Canada

395, rue Wellington  
Ottawa ON K1A 0N4  
Canada

**NOTICE:**

The author has granted a non-exclusive license allowing Library and Archives Canada to reproduce, publish, archive, preserve, conserve, communicate to the public by telecommunication or on the Internet, loan, distribute and sell theses worldwide, for commercial or non-commercial purposes, in microform, paper, electronic and/or any other formats.

The author retains copyright ownership and moral rights in this thesis. Neither the thesis nor substantial extracts from it may be printed or otherwise reproduced without the author's permission.

**AVIS:**

L'auteur a accordé une licence non exclusive permettant à la Bibliothèque et Archives Canada de reproduire, publier, archiver, sauvegarder, conserver, transmettre au public par télécommunication ou par l'Internet, prêter, distribuer et vendre des thèses partout dans le monde, à des fins commerciales ou autres, sur support microforme, papier, électronique et/ou autres formats.

L'auteur conserve la propriété du droit d'auteur et des droits moraux qui protègent cette thèse. Ni la thèse ni des extraits substantiels de celle-ci ne doivent être imprimés ou autrement reproduits sans son autorisation.

---

In compliance with the Canadian Privacy Act some supporting forms may have been removed from this thesis.

Conformément à la loi canadienne sur la protection de la vie privée, quelques formulaires secondaires ont été enlevés de cette thèse.

While these forms may be included in the document page count, their removal does not represent any loss of content from the thesis.

Bien que ces formulaires aient inclus dans la pagination, il n'y aura aucun contenu manquant.

  
**Canada**

---

# Contents

<b>Contents</b> . . . . .	ii
<b>List of Figures</b> . . . . .	iv
<b>List of Tables</b> . . . . .	viii
<b>Acknowledgements</b> . . . . .	ii
<b>Abstract</b> . . . . .	1
<b>1 Introduction</b> . . . . .	2
1.1 Modelling Rapidly Rotating Stars . . . . .	5
1.2 Synthetic Spectral Energy Distributions . . . . .	12
<b>2 The Codes</b> . . . . .	15
2.1 2-D Stellar Evolution: ROTORC . . . . .	16
2.2 Synthetic Atmospheres: PHOENIX . . . . .	23
2.3 The Atmospheric Integrator . . . . .	27
<b>3 Structure Models</b> . . . . .	38
<b>4 The Intensity Spectra</b> . . . . .	49
<b>5 Results and Discussion</b> . . . . .	54
<b>6 Conclusions</b> . . . . .	64

---

**Bibliography** ..... 66

# List of Figures

- 1.1 The structure of the models used by Roxburgh *et al.* (1965) and Sackmann & Anand (1970). In the outer region, the density is low and the gravitational potential behaves as that from a point mass at the centre of the star. In the inner region, the distortions must be small enough to be handled using a first-order approximation. From Roxburgh *et al.* (1965), with kind permission of Springer Science and Business Media. 7
- 1.2 Theoretical HR diagram, showing the position of zero-age main sequence models with increasing angular momentum. The numbers shown indicate the calculated equatorial velocities in  $\text{km s}^{-1}$ . The letters next to each line indicate the rotation law that produces each set of models. From Bodenheimer (1971), reproduced by permission of the AAS. . . . . 9
- 1.3 Cross-sections of four models produced by Jackson *et al.* (2004). Of these, model B seems to give the best match to the observed properties of Achernar. From Jackson *et al.* (2004), reproduced by permission of the AAS. . . . . 11
- 1.4 Theoretical line profiles for HeI  $\lambda 4471$ , FeI  $\lambda 4476$  and MgII  $\lambda 4481$  for a B3 type model at various values of  $i$ . The only broadening arises from rotation. From Collins & Sonneborn (1977), reproduced by permission of the AAS. . . . . 14
- 2.1 Fits to the instrumental profiles for spectrometer 1. The resulting fit gave a piecewise function used to convolve the PHOENIX intensity files. . . . . 28
- 2.2 Same as for Fig. 2.1 for spectrometer 2. . . . . 29

2.3	The integration mesh, shown over the upper hemisphere of the model. This mesh gives high spatial resolution over the surface of the star, increasing the accuracy of the integration. . . . .	31
2.4	Geometry required to determine the normal to the surface. The distance from the model centre to the surface at the location of interest is $R$ . This vector is extended by an arbitrary length $X$ . $R3$ is perpendicular to $X$ and is bounded by the vector $X$ and the surface normal. The vector $R2$ runs from the model centre to the intersection of $R3$ with the surface normal. Note that the vector in the direction of the observer could have a component outside the plane of the image. . . . .	32
2.5	Comparison between the integrated and convolved spectra produced by PHOENIX (dashed) and the code developed for this thesis (solid). The PHOENIX spectrum is integrated at $0.02 \text{ \AA}$ spacing and then convolved with the OAO-2 instrumental profile, while my integration convolves and then integrates on a $10 \text{ \AA}$ spacing. . . . .	35
2.6	Comparison of unconvolved output of the atmospheric integrator and the SED produced by PHOENIX. The difference indicates that the integration and the convolution do not commute perfectly. However, the difference is small. . . . .	36
2.7	The results of the interpolation test. The solid line represents the interpolated spectrum at 12000 K, the dashed line represents the spectrum produced from the PHOENIX intensity file at 12000 K and the dash-dot lines are the spectra at 13000 and 11000 K. . . . .	37
3.1	The distribution of angular momentum for the three power laws used: uniform rotation (solid), one described by Eqn. 3.1 (dashed) with $x = 0.6$ and one described by Eqn. 3.2 with $x = 1.4$ . . . . .	42
3.2	The evolution tracks of a $6.5 M_{\odot}$ (solid) and a $7.0 M_{\odot}$ (dashed) model. The observed location of Achernar is marked by a diamond. . . . .	43

3.3	The evolution of the axial ratios for the three models. Solid - 6.5 $M_{\odot}$ model with uniform rotation on the ZAMS; Dashed - power law defined by Eqn. 3.1; Dot-dashed - power law defined by Eqn. 3.2. Although the stars are initially quite oblate, they become much closer to spherical with age. . . . .	45
3.4	A cross sectional view of the photosphere of the SCF method model that most closely matches all the properties of Achernar. From Jackson <i>et al.</i> (2004), reproduced by permission of the AAS. . . . .	46
4.1	Comparison of LTE model atmospheres at $Z = 0.04$ (solid) and $Z = 0.02$ (dashed) for a uniform model with a temperature of 14000 K. . . . .	50
4.2	Synthetic intensity spectra generated using model atmospheres in LTE (solid line), with light elements in non-LTE (dashed line) and light elements and iron in non-LTE (dot-dashed line). The input model is a uniform spherical star with $T_{eff}$ of 15000 K and a metallicity of $Z = 0.02$ . . . . .	51
5.1	Synthetic flux spectra for a 6.5 $M_{\odot}$ model at inclinations of $0^{\circ}$ (top solid) $30^{\circ}$ (dashed) $60^{\circ}$ (dot dashed) and $90^{\circ}$ (lower solid). . . . .	55
5.2	Synthetic flux spectra for a 7 $M_{\odot}$ model at inclinations of $0^{\circ}$ (top solid) $30^{\circ}$ (dashed) $60^{\circ}$ (dot dashed) and $90^{\circ}$ (lower solid). . . . .	56
5.3	Polynomial fit to the averaged Ly $\alpha$ -Temperature data. This fit was then used to calculate an inferred temperature for the synthetic SEDs. . . . .	58
5.4	Top: The deduced effective temperature (dashed line) based on the synthetic SEDs as a function of inclination for the 6.5 $M_{\odot}$ model. The solid line shows the ROTORC effective temperature as a function of colatitude for the same model. The temperatures are evaluated at the midpoints of the $\theta$ zones of the Bottom: Same as for top plot, but for the 7 $M_{\odot}$ model. Both models are evolved to approximately match the observed properties of Achernar. . . . .	59

- 
- 5.5 The possible temperature and luminosity ranges of my models. The bold line shows the values for the  $6.5 M_{\odot}$  model, while the dash line shows the values for the  $7.0 M_{\odot}$  model. The circles and square show, from left to right, where a star would be observed if inclined at  $0, 30, 60$  and  $90^{\circ}$  for the  $6.5$  and  $7 M_{\odot}$  models respectively. The evolutionary sequences for uniformly rotating  $7 M_{\odot}$  and  $6.5 M_{\odot}$  models are shown for comparison. . . . . 61
- 5.6 The SED for a  $6.5 M_{\odot}$  model (solid) inclined at  $80^{\circ}$  and a  $7 M_{\odot}$  model (dashed) inclined at  $84^{\circ}$ . Although the structure of the two models is very different, there is little visible expression of this in the SED. However, both models are very different from the observed SED of Achernar (dot-dashed), particularly in the peak of the spectrum around  $1500 \text{ \AA}$  . . . . . 62
- 5.7 Same as for Fig. 5.6 but zoomed in to highlight the differences in the peak of the spectrum. . . . . 63

# List of Tables

2.1	Species treated in Non-Local Thermodynamic Equilibrium (NLTE) in the NLTE <sub>Light</sub> and NLTE <sub>Fe</sub> models. Each ionization stage is labeled with the number of energy levels and bound-bound transitions included in the statistical equilibrium rate equations. Note that this table shows only a sub-set of the total number of species that are currently treatable in statistical equilibrium by PHOENIX. . . . .	25
2.2	Levels of modeling realism. . . . .	26
2.3	The profile of the OAO-2 spectrometers, as given by Code & Meade (1979). . . . .	28
3.1	Properties of Achernar compared to typical B3 stars. The first two entries in the table are typical values for B3 stars, all others refer specifically to Achernar. . . . .	39
3.2	Properties of uniformly rotating models closest to Achernar. . . . .	40
3.3	Properties of models closest to Achernar with different rotation laws. . . . .	44
4.1	Mean abundances of B stars (from Gies & Lambert (1992) and Sofia & Meyer (2001)) compared to solar abundances. . . . .	52
5.1	Properties of models compared to the observed properties of Achernar . . . . .	63

# Acknowledgements

First, I would like to thank my supervisor, Dr. Bob Deupree. Without his support, guidance, and patience, this thesis would never have been written. I would also like to thank Dr. Ian Short for all his help with PHOENIX and modelling atmospheres, which turned out to be a much bigger part of this project than I anticipated. I would also like to thank Drs. Ian Short and David Guenther for being on my oral exam committee and my defense committee.

Thank you also to Dr. Gary Welch, who was able to explain how optical interferometry works. Thanks to him, the observations I based this project on are not quite so mysterious. Also, Drs. Art Code and Marilyn Mead were an invaluable source of information on the OAO-2 satellite. I would especially like to thank them for providing me with the reduced data in a text file format, saving me entering it all by hand. In trying to determine what metallicity I should use to model Achernar, Drs. Kim Venn and Amanda Karakas were both very helpful, providing me with many references and suggestions. I would also like to thank Birgit Fuhrmeister for help with PHOENIX.

I would also like to thank Jon, Ashley, Chris, Steve, Amanda, Chris, and Mina for being there with me through parts of the past two years. Thanks to all of you for helping me discover all that Halifax has to offer, and making sure I took advantage of some of it when things got really stressful.

# Abstract

## Models of Achernar: Evolution and Atmospheres of a rapidly rotating B Star

by Catherine Lovekin

**Abstract:** I investigate the effects of varying internal angular momentum distributions on the SEDs of massive stars. Rapidly rotating stars are deformed by rotation, and the degree of deformation can give us a further constraint on stellar evolution models, possibly allowing us to constrain the internal angular momentum distribution of these stars. I have modelled three different internal angular momentum distributions: uniform rotation and two different power law distributions. I use a fully implicit 2D stellar evolution code to determine the variation in surface properties exactly. The variation in surface properties of these evolutionary models are then used as the input for atmospheric modelling. I have made a grid of atmospheric intensities at values of  $T_{eff}$  and  $\log g$ , which I then use to interpolate the intensities in the direction of the observer over the surface of the star to produce a synthetic spectral energy distribution. I have used Achernar as a test case for this modelling.

July 29, 2005

# Chapter 1

## Introduction

To accurately model a non-rotating star, several pieces of physics must be known. The model must have accurate energy generation rates, taken from nuclear physics, opacities taken from atomic physics and an equation of state that describes the relationship between pressure and density inside the star. The switch to rotating stars does not require any new physics, but does require some additional information. The model must now be supplied with an angular momentum distribution. This is usually not known *a priori*, but is specified by the modeller. The addition of rotation to the stellar model adds terms to the existing stellar structure equations and requires some method for modelling the change in angular momentum with time. The most commonly used type of angular momentum distribution is solid body rotation, which assumes that the entire object rotates at the same angular velocity, regardless of distance from the axis of rotation. Some models also allow for differential rotation laws, where the angular velocity varies with position inside the star.

Rotation laws can be classified as either conservative or non-conservative. A conservative law is a law for which a potential can be derived from the angular velocity distribution. These include shellular rotation laws, which have constant angular momentum on spherical surfaces, and cylindrical rotation laws, where the law can be expressed as a function of the distance from the rotation axis,  $\varpi = r\sin\theta$ , where  $r$  is the local radius and  $\theta$  is the angle from the rotation axis.

Early-type stars tend to be rapid rotators, with  $v\sin i$  as high as 300-400 km s<sup>-1</sup> (Slettebak, 1949), where  $i$  is the inclination of the rotation axis of the star with respect to the observer. The rotational velocities of these O and B stars, while high, are not so high that the stars cannot be rotating as solid bodies. For massive stars, solid body rotation is a reasonable assumption. The main sequence lifetime of these stars is relatively short, and so the star is likely to stay well mixed,

maintaining solid body rotation. The only star for which astronomers have been able to determine the interior angular momentum distribution is the Sun, which is differentially rotating. However, the Sun is a low-mass star, so the arguments outlined above do not apply. It is also possible that the above argument is flawed, and that all stars exhibit differential rotation.

Of the early-type stars, the subgroup of Be stars tend to be the most rapidly rotating, with an average  $v \sin i$  as much as  $150 \text{ km s}^{-1}$  faster than for a similar group of B stars (Slettebak, 1949). The 'e' indicates that the Balmer lines in the stellar spectrum have been observed in emission at some time, probably produced by circumstellar activity. Otherwise, Be stars are, on average, relatively normal B stars, with no abnormalities in gravity, temperature or abundances (Porter & Rivinius, 2003). It was originally thought that Be stars are rotating at close to their critical velocities, the velocity at which the gravitational force and centrifugal force balance. Above this velocity, the star will begin to lose mass from the equator. Later studies by Slettebak (1949) seemed to indicate that these stars are rotating more slowly, at around 70-80 % of the critical velocity. Still more recent studies, see for example Townsend *et al.* (2004), have reopened the question, and the observed velocities may only give a lower limit on the rotation velocity (Porter & Rivinius, 2003). However, until recently, there was no evidence against early type stars undergoing solid body rotation.

Achernar ( $\alpha$  Eridani, HD10144) is a B3Ve star which does not seem to fit this picture. As the 9<sup>th</sup> brightest star in the sky, and the brightest Be star, it has been well studied. Both spectroscopic and photometric observations of this object date back to 1928, although it was not confirmed as a Be star until 1966 (Andrews & Breger, 1966). A star can be classified as a Be star and have a variable history of emission, as is the case for Achernar. The observations used in this thesis were all taken at times when there was no indication of emission lines in the spectra. For this reason, I feel confident that I can model Achernar as an ordinary B star. The fact that it is a Be star is incidental to this work, and is of interest only because it places the star in a more rapidly rotating subgroup. The observed  $v \sin i$  is  $225 \text{ km s}^{-1}$ , well within the normal range for Be stars. However, recent interferometric observations by Domiciano de Souza *et al.* (2003) have measured

the angular diameter as a function of orientation and determined the ratio of semimajor to semiminor axes to be  $a/b = 1.56 \pm 0.05$ , just over the theoretical limit for a rigid object rotating at critical velocity. Using the observed angular diameters and the Hipparcos parallax (Perryman *et al.*, 1997), the authors determined the equatorial radius of Achernar to be  $12.0 \pm 0.4 R_{\odot}$  and the maximum polar radius is  $7.7 \pm 0.2 R_{\odot}$ . Using these observations as constraints for a simple model designed to simulate interferometric observations, Domiciano de Souza *et al.* (2003) were able to show that this star could not be uniformly rotating. In reality, the problem is even worse. The value of  $7.7 R_{\odot}$  is the maximum polar radius, and assumes that the star is viewed with an inclination of  $90^{\circ}$ . If the star is viewed at some other inclination, as seems likely, the actual polar radius would be required to be even smaller to reproduce the observations.

My purpose is to see if I could produce a model of Achernar matching all the observational constraints, and possibly placing further constraints on the internal angular momentum distribution of the star. I used a 2D stellar evolution code (ROTORG), described in §2.1 to produce models with arbitrary internal angular momentum distributions. This modelling is described in Chapter 3.

I also attempted to reproduce the observed UV spectral energy distribution (SED) of Achernar. For comparison, I used the data taken by the OAO-2 satellite (Code & Meade, 1979). Although Achernar is a Be star, it has a variable history of emission. The OAO-2 satellite collected data from Dec. 1968 - Jan. 1973, times when no emission was observed (Balona *et al.*, 1986). Thus, the ultraviolet (UV) spectrum used in this project is thought to be that of the star itself, relatively uncontaminated by a circumstellar disk. This also means I do not have to model or compensate for the emission lines thought to be produced by the disk. The other set of observations used in this project are the interferometric observations of Domiciano de Souza *et al.* (2003). These observations were used to determine the projected shape of the star. If light from the circumstellar disk was present during these observations, light from the disk could make the equator of the star appear larger than it really is. To ensure that this was not the case, Domiciano de Souza *et al.* (2003) synthesized a  $H\alpha$  profile for the star and compared it to an observed spectrum taken during their

---

observing campaign. This allowed them to estimate the emission from the disk. The upper limit from this estimate was used to determine an upper limit on photospheric continuum flux emitted by the circumstellar envelope. This limit was estimated to be 12% of the total flux, indicating the circumstellar envelope was largely absent. The absence of a circumstellar envelope also indicates that the SED can be modelled based solely on the atmosphere of the star itself. To do this, I used the synthetic atmosphere code PHOENIX, described in more detail in §2.2, to produce a range of model atmospheres in temperature and effective gravity. I then wrote a separate code which interpolated between these models and integrated over the surface of the star to find the SED, described in §2.3. The modelling process and results are described in Chapters 4 and 5 respectively.

In the next sections, I describe some of the historical research in modelling rotating stars and generating synthetic SEDs.

## 1.1 Modelling Rapidly Rotating Stars

One of the first studies on the effects of rotation on a main sequence star was performed by Sweet & Roy (1953). Their calculations were based on first-order perturbations of a rotating Cowling model. The Cowling model is an analytic solution to the equations of stellar structure with a convective core and a radiative envelope. The first order perturbation model breaks down when the ratio of the centrifugal force to the gravitational force exceeds 0.29, as the perturbations become large enough that higher order effects must be taken into account. These calculations show that the mean effective temperature is reduced by rotation, as is the total luminosity. However, when viewed pole-on, the apparent luminosity of the star is increased. The result of these effects is that the observed rotation rates could result in a spread in luminosity on the order of half a magnitude depending on the inclination of the star, although this is approached only for the most rapidly rotating B stars.

Later, rapid rotation in a main sequence star was studied by Roxburgh *et al.* (1965). These models divided the star into two regions, as illustrated in Fig. 1.1. The outer region is assumed to

have negligible mass, so its gravitational potential is due primarily to the inner region. The potential in the outer region is given by an approximate solution of Laplace's equation over this region. Once the potential is known, the structure equations can be integrated, following the the same method as for spherically symmetric models. In the inner region, the ratio of the centrifugal force to gravity is small compared to unity everywhere, so this region can be modelled using first order perturbation techniques. The physics used in these models includes only electron scattering for opacity, which applies to very early-type stars, while at the same time neglecting radiation pressure, which applies only to late-type stars. More realistic opacities and improved nuclear energy generation rates were included in an extension to this method by Faulkner *et al.* (1968).

More realistic models for slow, uniformly rotating stars including convection were calculated using first order perturbation theory by Sackmann & Anand (1969). These models included the effects of radiation pressure, which can be significant in early-type stars. Sackmann & Anand (1969) use the same underlying structure model illustrated in Fig. 1.1. The models described above assume that the star can be modelled using equipotentials that are only slightly different from simple surfaces, i.e., spheres or spheroids. This assumptions limits the method to stars that are only slightly distorted and do not have large changes in their internal structure or luminosity (Ostriker & Mark, 1968). It is also possible to take the potential as a given function, avoiding some of the difficulties normally involved in solving for the total potential of the star. By assuming the potential can be modelled as a Roche potential due to a point source, astronomers can model the outer envelope with the methods described above. However, the regions treated in this way must be small in mass when compared to the whole star.

The structure and evolution of rapidly rotating B stars was calculated by Sackmann & Anand (1970). For uniformly rotating models, rotation can decrease the luminosity by about 7%. The effective temperature also decreases slightly, shifting the evolutionary sequence of the star down and to the right in the Hertzsprung-Russel (HR) diagram.

The self consistent field (SCF) method (Ostriker & Mark, 1968) has also been used to model

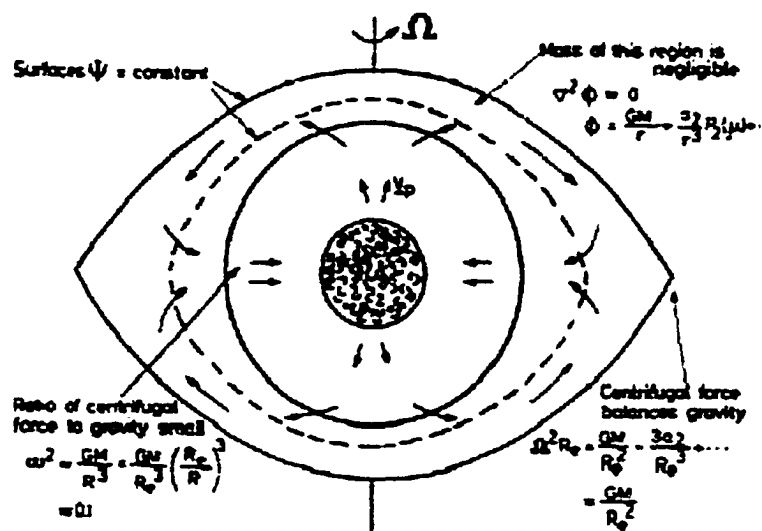


Figure 1.1: The structure of the models used by Roxburgh *et al.* (1965) and Sackmann & Anand (1970). In the outer region, the density is low and the gravitational potential behaves as that from a point mass at the centre of the star. In the inner region, the distortions must be small enough to be handled using a first-order approximation. From Roxburgh *et al.* (1965), with kind permission of Springer Science and Business Media.

---

rapidly rotating stars. Mark (1968) used this method to model rapidly rotating stars with masses of  $28.25 M_{\odot}$  and  $62.7 M_{\odot}$ . The SCF method uses an iterative approach to solve for hydrostatic equilibrium and Poisson's equation for gravitational potential. As originally designed, the SCF method only considered the hydrostatic structure of the star. This method was extended by Jackson (1970) to include the Henyey method for solving all the equations of stellar structure. The early versions of this method ran into convergence difficulties below  $9 M_{\odot}$  (Clement, 1978), even for non-rotating models. This method also restricts the type of rotation laws allowed, as the angular momentum must be constant on cylindrical surfaces parallel to the rotation axis (Mark, 1968).

Studies with other rotation laws seem to find larger shifts in the stellar parameters. The effects of rapid rotation have also been studied by Bodenheimer (1971), using the SCF method to compute the two-dimensional structure of stars of  $15$ ,  $30$  and  $60 M_{\odot}$ . These models use four different conservative rotation laws. The results for zero age main sequence (ZAMS) models agrees qualitatively with those of Sackmann & Anand (1970), with luminosity decreasing as the angular momentum increases. A sample of their results is shown in Fig. 1.2.

A third method for modeling rapidly rotating stars has been described by Clement (1974, 1978, 1979). This method involves solving Poisson's equation using a two dimensional finite-difference technique. This method only allows conservative rotation laws. If non-conservative rotation laws are used, the calculation becomes numerically unstable.

The effects of differential rotation have been studied by Collins & Smith (1985), using a cylindrical rotation law applied to A stars. The interiors of these stars were modelled using a 1D stellar model with three correction factors applied to account for the differential rotation.

In this thesis, I take these models one step further, applying a fully implicit 2D stellar evolution code, described more fully in section 2.1, with arbitrary rotation laws to produce the interior models. Using a 2D evolution code to produce the interior models allows me to determine the surface variations directly, rather than having to assume uniform surface velocity or using von Zeipel's law (von Zeipel, 1924). I can also calculate the true gravitational potential for my models directly, eliminating

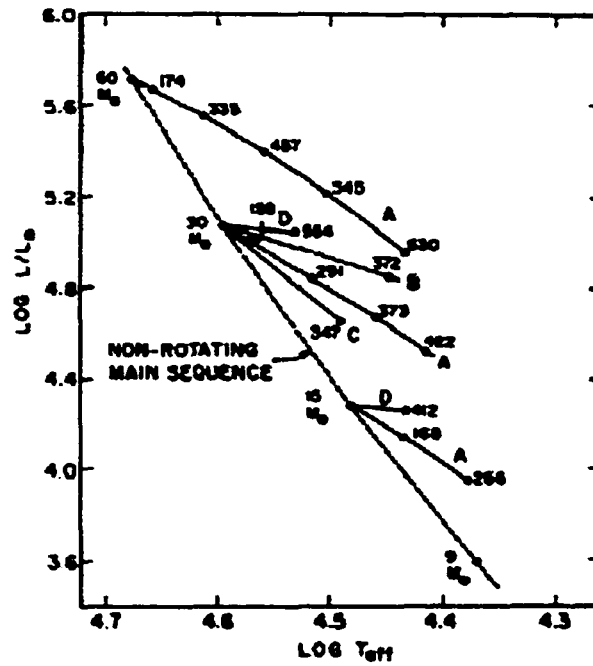


Figure 1.2: Theoretical HR diagram, showing the position of zero-age main sequence models with increasing angular momentum. The numbers shown indicate the calculated equatorial velocities in  $\text{km s}^{-1}$ . The letters next to each line indicate the rotation law that produces each set of models. From Bodenheimer (1971), reproduced by permission of the AAS.

the need to assume a Roche potential, as for the two region model described in Fig. 1.1.

More recently, a finite difference method for two dimensional stellar evolution has been developed by Deupree (1990). This is the method used in this thesis, and will be described in more detail in §2.1.

Ours is not the first attempt to model Achernar. Models of the surface shape are compared to the observations in Domiciano de Souza *et al.* (2003) and the models are described in more detail in Domiciano de Souza *et al.* (2002). This model assumes uniform rotation and a point mass gravitational potential. This model is not intended to accurately model the structure and evolution of a star, but rather is intended for comparison to the interferometric observations.

Since the interferometric measurements of the oblateness of Achernar were made, Jackson *et al.* (2004) have also attempted to model the star using an updated version of the SCF method. These revisions allow stars with mass less than  $9M_{\odot}$  to converge. The new SCF method is described in detail in Jackson *et al.* (2005). To model Achernar, Jackson *et al.* (2004) studied ZAMS models between 6 and  $15 M_{\odot}$ , with the internal angular momentum as a function of distance from the rotation axis ( $\Omega(\varpi)$ ) described by

$$\Omega(\varpi) = \frac{\Omega_o}{1 + (\varpi/\varpi_{1/2})^2}. \quad (1.1)$$

where  $\varpi_{1/2} = R_{eq}/\alpha$ ,  $R_{eq}$  is the surface equatorial radius and  $\Omega_o$  and  $\alpha$  are free parameters. Their best match to Achernar occurs at a mass of  $9M_{\odot}$ , with  $\alpha = 2$  and  $\eta = 4.9$ , where  $\eta = \Omega_o/\Omega_{crit}$ .  $\Omega_{crit}$  is the equatorial angular velocity at which the centrifugal and gravitational forces are equal. Note that this definition of  $\eta$  is different from the definition used elsewhere in this thesis. This model has  $\log(L/L_{\odot}) = 3.51$ ,  $R_{eq} = 11.73R_{\odot}$ ,  $R_p = 0.29R_{eq}$ ,  $\langle T_{eff} \rangle = 14800$  and  $v_{eq} = 375 \text{ km s}^{-1}$ , in good agreement with the theoretical values for Achernar (see Table 3.1). At this point, the star is very deformed (see Fig. 1.3) and one must question how deformed an object can be and still fit the traditional definition of a star.

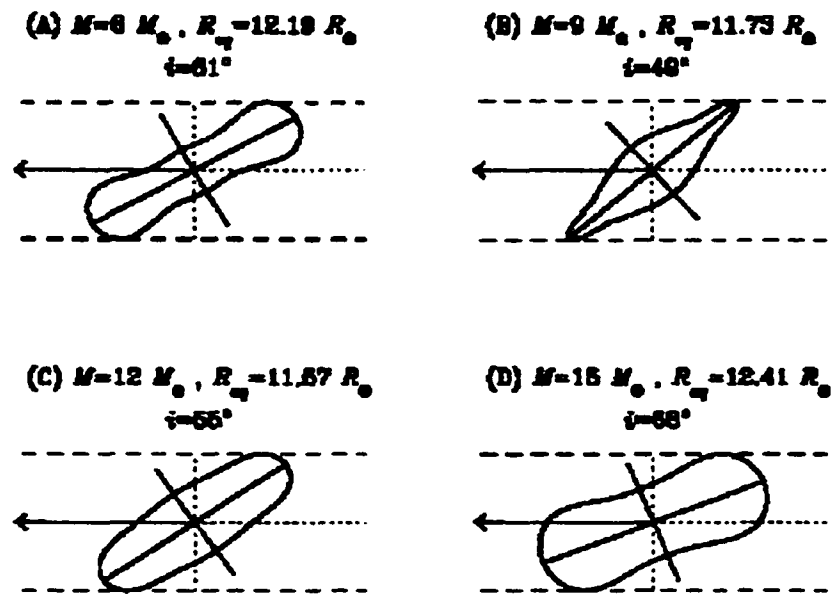


Figure 1.3: Cross-sections of four models produced by Jackson *et al.* (2004). Of these, model B seems to give the best match to the observed properties of Achernar. From Jackson *et al.* (2004), reproduced by permission of the AAS.

## 1.2 Synthetic Spectral Energy Distributions

Stellar theorists describe stars in terms of their intrinsic properties, such as mass, effective temperature and luminosity, but it is difficult to determine these quantities directly from observations of stars, as they depend on the inclination and distance to the star. To compare models with observations, the internal and atmospheric model parameters, such as effective temperature and surface gravity, must be translated into observational quantities (e.g., flux). This translation is one-to-one for spherically symmetric stars, for which the effective temperature and gravity are the same everywhere on the surface, and their relationship with luminosity is well defined, but becomes more difficult for rotating stars, where both temperature and gravity vary over the surface of the star. If the surface equipotential is similar in shape to the interior equipotentials, this surface variation can be described using von Zeipel's law (von Zeipel, 1924), where the local radiative flux is proportional to the local effective gravity, which is the sum of the force of gravity and the centrifugal force. Thus,  $T_{eff} \propto g_{eff}^{1/4}$ , which suggests that the spectrum of a rapidly rotating star is the integral of the temperature-dependent intensity over the surface of the star. Because the observed composite spectrum will vary with inclination, the values of  $T_{eff}$  and  $\log g$  derived from observations will also depend on the inclination of the rotation axis with respect to the observer, something that is not known *a priori*.

A corollary of von Zeipel's law is that the relationship between the luminosity and observed bolometric magnitude of a star also depends on the inclination, as the amount of energy radiated per unit area from the stellar surface also varies with colatitude. Thus, even something as relatively straightforward as assigning a location in the HR diagram is not simple for rotating stars, as the location would not be a point but a curve with inclination as the free parameter. The length and shape of the curve depends on the amount of surface rotation and perhaps the angular momentum distribution. The inclination determines where on the curve the observer would place the star. This effect has been well studied (Maeder & Peytremann, 1970; Hardorp & Strittmatter, 1968; Collins,

---

1966). Maeder & Peytremann (1970) studied stars with varying rotational velocity on the ZAMS. The resulting curve is nearly parallel to the main sequence. This was the first group to include opacities due to specific lines in their models, rather than just including the continuum opacity, as was done by Hardorp & Strittmatter (1968) and Collins (1966). Maeder & Peytremann (1970) also included the effects of hydrogen line opacities due to the Balmer and Lyman series. The stellar interior models are based on those described by Roxburgh *et al.* (1965). The atmospheres were constructed assuming local thermodynamic equilibrium (LTE).

I have also used my models to test the predictions of von Zeipel's law for rapidly rotating stars with both uniform and differential rotation laws. The results indicate that von Zeipel's law gives reasonably accurate predictions as long as the interior mass is not significantly asymmetrical. This work is discussed in Lovekin *et al.* (2005), but will not be included in this thesis. The observed spectral energy distribution (SED) can be found from the weighted integral of the radiative intensities emitted in the direction of the observer, integrated over the surface of the star. In principle, the SED contains information about the angular variation of the quantities which influence the radiation field. The general method for calculating the SED is well known and has been used in many prior investigations. First, interior models must be produced to give the surface structure of the star. Then, a model atmosphere program must be used to simulate the observed SED. These results can then be used to examine individual lines, as was done by Collins (1974) and Collins & Sonneborn (1977), or the overall SED of the star, as done by Linnell & Hubeny (1994). The information in the lines may give more indication than the overall SED as to the rotational structure of the star, as shown in Fig. 1.4. However, the lines shown here are unbroadened. Since B stars undergo significant rotation, the resultant Doppler broadening may erase this information.

I chose here to work with the SED rather than individual lines, as was done by Collins (1974) and Collins & Sonneborn (1977) because I hoped to be able to employ this method as a general technique over a wide range of stars. I also hoped to avoid dependence on the properties of any particular set of lines.

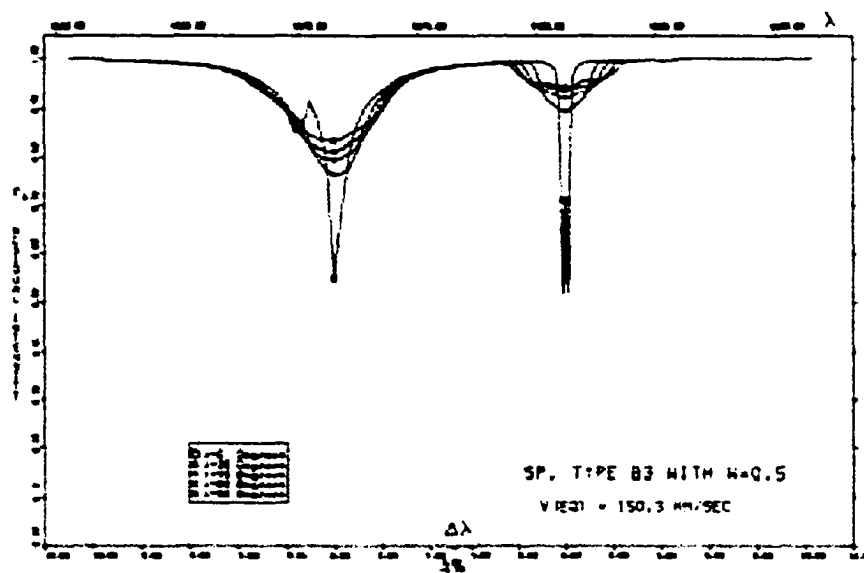


Figure 1.4: Theoretical line profiles for HeI  $\lambda 4471$ , FeI  $\lambda 4476$  and MgII  $\lambda 4481$  for a B3 type model at various values of  $i$ . The only broadening arises from rotation. From Collins & Sonneborn (1977), reproduced by permission of the AAS.

---

## Chapter 2

# The Codes

There are three numerical modelling components required to produce a synthetic SED for a rotating star. The first is the calculation of fully 2-D stellar evolution sequences with rotation (Deupree, 1990, 1995, 1998) to obtain the effective temperatures and effective surface gravities as functions of latitude for any point in a stellar evolution sequence. These models can be significantly deformed by rotation, so the effective temperature and effective surface gravity are not uniform over the surface of the star. I define the effective temperature as the temperature required to produce the local surface flux assuming the flux is black body. The effective gravity is defined as the component of the vector sum of the centrifugal force and the gradient of the gravitational potential normal to the local surface (i.e., the local vertical).

The second modelling component is the atmosphere of the star. I assume that I can model the atmosphere at any given location on the surface as flat slab of uniform thickness in which the parameters depend only on the depth, known as a plane parallel atmosphere, with the local effective temperature and effective gravity. This plane parallel approximation is good if the horizontal photon mean free path is very small compared to the horizontal distance over which there are significant structural changes along the stellar surface. The region where this approximation is least reliable is near the equator, where the effective gravity is smallest and the horizontal structural gradients the largest. This error is balanced somewhat by the fact that the equatorial region has the lowest effective temperature, so it contributes less to the observed flux except at inclinations of nearly ninety degrees.

I calculated a grid of model atmospheres that cover the range of effective temperatures and effective gravities required. For this I used the PHOENIX model atmosphere code (Hauschildt &

Baron, 1999). I used these models to calculate the emergent intensities as a function of angle from the vertical. I then integrated these intensities to obtain the observed flux.

The third modelling component is the numerical integration of these intensities over the stellar surface to obtain the observed flux. The procedure used is very similar to that described by Linnell & Hubeny (1994) and Cassinelli (1987). The surface of the star is divided into a mesh in longitude and latitude. For a given inclination the direction to the observer can be calculated at any location on the surface and the appropriate intensity selected from the input supplied by the model atmosphere code. This intensity is then multiplied by the local surface area element and the cosine of the angle between the local surface normal and the direction to the observer. The sum of the intensities produced by all the mesh zones gives the spectral energy distribution of the star at a given inclination. Before integration, the intensities are convolved with the profile of the OAO-2 spectrometers. This profile covers too large a wavelength range (10-20 Å) for Doppler shifts to be noticeable. For this reason, the Doppler shift has been neglected in this integration.

## 2.1 2-D Stellar Evolution: ROTORC

The surface variation of  $T_{eff}$  and  $g_{eff}$  is taken from evolution sequences computed with a 2.5D stellar evolution code, ROTORC (Deupree 1990, 1995, 1998). This code uses the fractional radius,  $x = r/R$ , and the colatitudinal variable,  $\theta$ , as the independent variables in the stellar structure equations rather than  $M_r$ , as is usually the case for one dimensional codes. To relate  $M_r$  to  $r$  in a 2D code would require taking the angular average over the density distribution, making it awkward for the independent variable. The code uses a separate equation for each component of the momentum. This allows there to be some component of motion in the azimuthal direction ( $\phi$ ), although this motion is constrained to be azimuthally symmetric, accounting for the extra half dimension. All calculations are performed in an inertial frame of reference, so the azimuthal momentum allows for evolution of the internal rotation profile without requiring it to be uniform, or even conservative. In

two dimensions, there are seven stellar structure equations, as opposed to four equations for the more common one dimensional calculation. The equations used and the differences from 1D calculations are described below. The first equation is mass conservation, which when written in 2D becomes:

$$R \frac{\partial \rho}{\partial t} + (v_r - V_o) \frac{\partial \rho}{\partial x} + \frac{v_\theta}{x} \frac{\partial \rho}{\partial \theta} + \frac{\rho}{x^2} \frac{\partial}{\partial x} (x^2 v_r) + \frac{\rho}{x \sin \theta} [(\sin \theta) v_\theta] = 0 \quad (2.1)$$

The major difference between the 1D and 2D equations is found in the equation(s) for momentum conservation. In 1D, there is only one equation. For my 2D calculation, I keep track of all three components, as described above. These three equations then become

$$R^2 \frac{\partial v_r}{\partial t} + R(v_r - V_o) \frac{\partial v_r}{\partial x} + \frac{R v_\theta}{x} \frac{\partial v_r}{\partial \theta} + \frac{R \partial P}{\rho \partial x} + R \frac{\partial \Phi}{\partial x} - R \frac{v_\phi^2}{x} - R \frac{v_\theta^2}{x} = 0 \quad (2.2)$$

$$R^2 \frac{\partial v_\theta}{\partial t} + R(v_r - V_o) \frac{\partial v_\theta}{\partial x} + \frac{R v_\theta}{x} \frac{\partial v_\theta}{\partial \theta} + \frac{R \partial P}{\rho x \partial \theta} + \frac{R \partial \Phi}{x \partial \theta} - R \frac{v_\phi^2}{x} \cot \theta + R \frac{v_r v_\theta}{x} = 0 \quad (2.3)$$

$$R^2 \frac{\partial v_\phi}{\partial t} + R(v_r - V_o) \frac{\partial v_\phi}{\partial x} + \frac{R v_\theta}{x} \frac{\partial v_\phi}{\partial \theta} + R \frac{v_r v_\theta}{x} + R \frac{v_\theta v_\phi}{x} \cot \theta = 0 \quad (2.4)$$

for the  $r$ ,  $\theta$ , and  $\phi$  components respectively. Next is the equation for energy conservation. As this code is designed to perform both hydrodynamic simulations and evolution calculations, both radiative transport and convective transport have been combined into a single equation. This required modifying the effective opacity, as described later in this section. The modified equation becomes:

$$\begin{aligned} R^2 \frac{\partial E}{\partial t} + R(v_r - V_o) \frac{\partial E}{\partial x} + \frac{R v_\theta}{x} \frac{\partial E}{\partial \theta} - \frac{R^2 P}{\rho x^2} \frac{\partial}{\partial x} (x^2 v_r) - \frac{R^2 P}{\rho x \sin \theta} \frac{\partial}{\partial \theta} [(\sin \theta) v_\theta] \\ - R^2 \epsilon - \frac{r \sigma}{4 \rho x^2} \frac{\partial}{\partial x} \left( \frac{x^2 \partial T^4}{\rho \kappa \partial x} \right) - \frac{4 \sigma}{3 \rho x^2 \sin \theta} \frac{\partial}{\partial \theta} \left( \frac{\sin \theta \partial T^4}{\kappa \rho \partial \theta} \right) = 0 \end{aligned} \quad (2.5)$$

In two dimensions, Poisson's equation for the gravitational potential ( $\Phi$ ) becomes:

$$\frac{1}{x^2} \frac{\partial}{\partial x} \left( x^2 \frac{\partial \Phi}{\partial x} \right) + \frac{1}{x^2 \sin \theta} \frac{\partial}{\partial \theta} \left( \sin \theta \frac{\partial \Phi}{\partial \theta} \right) - 4\pi G \rho R^2 = 0 \quad (2.6)$$

Use of the Henyey method (described below) requires the composition equation to be solved simultaneously with the other stellar structure equations. This seventh equation is not a stellar structure equation, but is required for time-dependent evolution. In 2D, the hydrogen composition obeys the following equation:

$$R \frac{\partial X}{\partial t} + (v_r - V_o) \frac{\partial X}{\partial x} + \frac{v_\theta}{x} \frac{\partial X}{\partial \theta} + Rq = 0 \quad (2.7)$$

In this system,  $V_o$  is the radial flow velocity of the coordinate system,  $P$  is the pressure,  $E$  is the specific internal energy,  $T$  is the temperature,  $\rho$  is the density,  $X$  is the hydrogen mass fraction and  $q$  is the nuclear destruction rate of hydrogen. In this formulation,  $P$ ,  $E$ ,  $X$  and  $q$  are all functions of  $\rho$ ,  $T$  and  $x$ .  $\rho$  and  $T$  are assumed to be uniform with respect to  $\phi$  and are functions of  $x$  and  $\theta$  only. The boundary conditions at the centre are

$$\frac{\partial P}{\partial r} = 0 \quad \text{at} \quad r = 0, \quad (2.8)$$

$$\text{Radial flux} = 0 \quad \text{at} \quad r = 0, \quad (2.9)$$

and

$$\frac{\partial \Phi}{\partial r} = 0 \quad \text{at} \quad r = 0. \quad (2.10)$$

where  $\Phi$  is the gravitational potential. At the stellar surface

$$\rho = \rho_{ref}, \quad (2.11)$$

$$\Phi = \Phi_{ext}, \quad (2.12)$$

and

$$\text{Flux} = 2\sigma T_s^4, \quad (2.13)$$

where  $\rho_{ref}$  is a reference density,  $T_s$  is the surface temperature and  $\Phi_{ext}$  is the gravitational potential at the surface evaluated on a spherical surface exterior to the star. I assume an Eddington atmosphere, so  $T_{eff} = \sqrt[4]{2}T_s$ . I impose symmetry at  $\theta = 0$  and  $\theta = \pi/2$ , which requires that  $v_\theta = 0$  and

$$\frac{\partial \rho}{\partial \theta} = \frac{\partial T}{\partial \theta} = \frac{\partial \Phi}{\partial \theta} = \frac{\partial v_r}{\partial \theta} = \frac{\partial v_\phi}{\partial \theta}. \quad (2.14)$$

The total mass of the model is given by

$$M - 2\pi R^3 \int_{x=0}^1 \int_{\theta=0}^{\pi} \rho x^2 \sin\theta d\theta dx = 0. \quad (2.15)$$

with the double integral replaced by a sum over the 2D mesh. Equations 2.1 - 2.7 are then solved simultaneously and implicitly using a 2D version of the Henyey technique (Henyey *et al.*, 1964). In this method, the first order perturbations to the finite difference representations of equations 2.1 -

2.7 can be reduced to a matrix equation of the form

$$\mathbf{A}\delta q_{i-1,j} + \mathbf{B}\delta q_{i,j-1} + \mathbf{C}\delta q_{i,j} + \mathbf{D}\delta q_{i,j+1} + \mathbf{E}\delta q_{i+1,j} + \mathbf{F}\delta R + \mathbf{G} = 0, \quad (2.16)$$

where  $\delta q_{i,j}$  is a column vector containing the perturbations of the integration variables ( $P, T, v_r, v_\theta, v_\phi, \Phi$  and  $X$ ). This equation can be solved by applying the inner boundary conditions at  $i = 1$  and iterating from  $i = 2$  to  $n - 1$  to get expressions for the coefficients. Applying the outer boundary conditions at  $n$  solves for the coefficients, which can then be applied recursively from  $n - 1$  to 1 to find the values of  $\delta q_{i,j}$ .

The 2D stellar surface is defined to be on a surface given by

$$\psi = \Phi - \frac{1}{2}v_\phi^2. \quad (2.17)$$

I shall call  $\psi$  the total potential, although this is strictly true only if the centrifugal force is conservative. The surface potential is calculated at  $x = 1$  at the equator and the surface is taken as the radial zone with the value of  $\psi$  closest to the equatorial value for all other angular zones. In general, the gravitational potential is calculated using Poisson's equation with the surface potential boundary condition at each latitude being determined by the suitably weighted integral over the interior mass. The local effective temperature is calculated as the value required to transmit the flux through the local surface of the star and is calculated at each latitude. The overall effective temperature (the 'ROTORC' or 'evolutionary' temperature) is calculated based on the total luminosity and surface area of the model.

To understand the numerical method, consider a differential equation of the form:

$$\frac{\partial f}{\partial x} = g(x, f). \quad (2.18)$$

In finite difference form, this equation can be expressed in one of two ways:

$$\frac{f^{n+1} - f^n}{\Delta x} = g(x, f^n) \quad (2.19)$$

or

$$\frac{f^{n+1} - f^n}{\Delta x} = g(x, f^{n+1}). \quad (2.20)$$

The first form of these is much simpler and can be solved directly for  $f^{n+1}$ . However, using  $f^n$  on both sides of the solution means that the solution can become unstable if the time step is too large. The limit on the timestep is known as the Courant condition (Richtmyer & Morton, 1957). This method of solution is called an explicit solution. The second form, the implicit solution, is much more difficult to solve, but has some significant advantages. There is no constraint imposed on the timestep by stability requirements, as discussed in more detail below.

These finite difference calculations can be done in one of two coordinate systems, either Lagrangian or Eulerian. In a Lagrangian system, the code keeps track of the individual fluid elements as they move around, and the coordinate system flows with individual elements. The equations in this system are straightforward, for example:

$$\frac{d\rho}{dt} = -\rho \frac{du}{dx} \quad (2.21)$$

where  $u$  is the velocity of the fluid. Because the coordinate system can change as the calculation proceeds, the flow of the fluid may produce a coordinate system inappropriate for the calculation being done. In this case, the calculation must be stopped and the coordinate system reset. This is one of the main disadvantages to using Lagrangian calculations to model fluid systems, such as stars. In contrast, in an Eulerian system, the code uses a fixed coordinate system and tracks how the fluid elements move around within the fixed system. This introduces extra terms into the equations, for

example:

$$\frac{\partial \rho}{\partial t} + u \frac{\partial \rho}{\partial x} = -\rho \frac{\partial u}{\partial x} \quad (2.22)$$

This extra term is known as an advection term. This term gives rise to some inaccuracies in the calculation. There are various techniques for minimizing this inaccuracy, but it cannot be removed entirely. ROTORC, uses a combination of the two schemes. In the  $\theta$  direction, the code uses an Eulerian system. In the radial direction, the code uses a directed-flow coordinate system, which is neither Eulerian nor Lagrangian. This system allows the coordinate system to flow in a prescribed manner, rather than freely as in a true Lagrangian calculation.

Because ROTORC is fully implicit, there are no stability constraints on the time step. However, there are accuracy constraints. Some inaccuracy arises as a result of the advection terms in any non-Lagrangian calculation. If I use the conservation equations for composition or angular momentum in the convective core, the code is forced to follow the evolution on a timescale short enough to follow the convective mixing. To avoid this, I force the convective core to be of uniform composition. As the evolution continues, the core is chemically uniformly mixed but angular momentum is not redistributed.

Typically, when modelling convection, the logarithmic gradient of the temperature with respect to pressure is forced to be the minimum of the radiative or adiabatic gradients, i.e.

$$\frac{d \ln T}{d \ln P} = \min(\nabla_{ad}, \nabla_{rad}) \quad (2.23)$$

If this formulation were to be used here, equation 2.5 would need to be replaced with an equation unsuitable for dynamic calculations, or modified to be compatible with equation 2.23. This first option precludes switching between evolutionary and hydrodynamic calculations without switching equations. At the time of the switch, both equations would not necessarily be satisfied, which could

produce unrealistic results. The adopted solution is to define an effective opacity

$$\kappa_{eff} = \kappa \cdot \frac{\nabla_{ad}}{\nabla_{rad}} \quad \text{if} \quad \nabla_{ad} \leq \nabla_{rad}, \quad (2.24)$$

where  $\kappa_{eff}$  is the opacity used in equation 2.5 and  $\kappa$  is the actual radiative opacity.

All models calculated here included convective core overshooting of 0.38 times the e-folding distance of the pressure evaluated at the convective core boundary, based on the 2D hydrodynamic simulations of Deupree (2000, 2001). Although the amount of overshooting can affect the evolution of the star, I do not expect this to play any role in my study on the surface effects of rotation. The radiative opacities and equation of state are looked up and interpolated from the OPAL tables (Iglesias & Rogers, 1996). The models here were calculated by conserving angular momentum at each point in the star (“local” conservation of angular momentum) throughout the evolution. The convective core could also be modelled by forcing it to be uniformly rotating. The difference between these two treatments is small, as until the very end of the main sequence, the structure of the convective core does not change significantly. As a result, the angular momentum distributions resulting from either uniform rotation or local conservation of angular momentum are nearly the same.

## 2.2 Synthetic Atmospheres: PHOENIX

Stellar interior models use a one zone atmosphere to determine the effective temperature of a star, but this cannot give details on the spectral energy distribution observed. To do this, I must use a code that can model the atmosphere of the star and solve the equation of radiative transfer

$$\frac{dI_\nu}{d\tau_\nu} = I_\nu - \frac{j_\nu}{\kappa_\nu} \quad (2.25)$$

where  $j_\nu/\kappa_\nu$  is called the source function,  $S(\nu)$ ,  $j_\nu$  is the emission coefficient,  $\kappa_\nu$  is the absorption coefficient or opacity and  $\tau_\nu$  is the optical depth.

Such an atmosphere code must be capable of keeping track of the populations in thousands of energy levels of the atomic elements. This can be done either by assuming the states are populated according to local thermodynamic equilibrium (LTE) or by modelling the states more realistically in non-LTE (NLTE). In LTE, matter and radiation are assumed to be in equilibrium with each other locally everywhere. The source function for the radiation can easily be described by the Planck function,  $B(\lambda, T)$ , and levels are populated according to Maxwell-Boltzmann statistics. When non-LTE effects are taken into consideration, the situation becomes more complicated, because the interactions between matter and radiation must be calculated to determine the source function and properly model the radiation field.

I use PHOENIX to calculate plane-parallel atmospheres in both LTE and non-LTE and generate the intensity fields used to produce my synthetic energy distributions (see §2.3). PHOENIX makes use of a fast and accurate technique called the Operator Splitting/Accelerated Lambda Iteration (OS/ALI) scheme to solve self-consistently the radiative transfer equation and the NLTE statistical equilibrium (SE) rate equations for many species of atoms and overlapping transitions (Hauschildt & Baron, 1999) in a stellar atmosphere. This method iterates on the zeroth angular moment of  $I_\nu$  or the mean intensity

$$J_\nu = \frac{1}{2} \int_{-1}^1 d\mu I_\nu \quad (2.26)$$

and the source function,  $S_\nu$ . The formal solution to the radiative transfer equation (Eqn. 2.25) relates the mean intensity and the source function by use of the operator  $\Lambda$  by

$$J_\nu = \Lambda(S_\nu) \quad (2.27)$$

Table 2.1: Species treated in Non-Local Thermodynamic Equilibrium (NLTE) in the NLTE<sub>Light</sub> and NLTE<sub>Fe</sub> models. Each ionization stage is labeled with the number of energy levels and bound-bound transitions included in the statistical equilibrium rate equations. Note that this table shows only a sub-set of the total number of species that are currently treatable in statistical equilibrium by PHOENIX.

Element	Model	Ionization Stage			
		I	II	III	IV
H	NLTE <sub>Light</sub> , NLTE <sub>Fe</sub>	80/3160	...	...	...
He	NLTE <sub>Light</sub> , NLTE <sub>Fe</sub>	19/37	10/45	...	...
Li	NLTE <sub>Light</sub> , NLTE <sub>Fe</sub>	57/333	55/124	...	...
C	NLTE <sub>Light</sub> , NLTE <sub>Fe</sub>	228/1387	85/336	79/365	...
N	NLTE <sub>Light</sub> , NLTE <sub>Fe</sub>	252/2313	152/1110	87/266	...
O	NLTE <sub>Light</sub> , NLTE <sub>Fe</sub>	36/66	171/1304	137/765	...
Ne	NLTE <sub>Light</sub> , NLTE <sub>Fe</sub>	26/37	...	...	...
Na	NLTE <sub>Light</sub> , NLTE <sub>Fe</sub>	53/142	35/171	...	...
Mg	NLTE <sub>Light</sub> , NLTE <sub>Fe</sub>	273/835	72/340	91/656	...
Al	NLTE <sub>Light</sub> , NLTE <sub>Fe</sub>	111/250	188/1674	58/297	31/142
Si	NLTE <sub>Light</sub> , NLTE <sub>Fe</sub>	329/1871	93/436	155/1027	52/292
P	NLTE <sub>Light</sub> , NLTE <sub>Fe</sub>	229/903	89/760	51/145	50/174
S	NLTE <sub>Light</sub> , NLTE <sub>Fe</sub>	146/439	84/444	41/170	28/50
K	NLTE <sub>Light</sub> , NLTE <sub>Fe</sub>	73/210	22/66	38/178	...
Ca	NLTE <sub>Light</sub> , NLTE <sub>Fe</sub>	194/1029	87/455	150/1661	...
Fe	NLTE <sub>Fe</sub>	494/6903	617/13675	566/9721	243/2592

The method of solution requires an initial guess to  $S_\nu$  and iterates the  $\Lambda$  operation by

$$J_{new} = \Lambda S_{old} \quad S_{new} = (1 - \epsilon) J_{new} + \epsilon B \quad (2.28)$$

where  $\epsilon$  is the thermal coupling parameter and  $B$  is the Planck function. The operator splitting involves redefining  $\Lambda = \Lambda^* + (\Lambda - \Lambda^*)$  and substituting into Eqn. 2.28.  $\Lambda^*$  is an approximate  $\Lambda$ -operator, which if chosen wisely, can greatly increase the efficiency of the solution.

Recently Short *et al.* (1999) have greatly increased the number of species and ionization stages treated in SE by PHOENIX. At least the lowest two levels of 24 elements, including the lowest six ionization stages of the 20 most important elements, including Fe and four other Fe-group elements, can now be treated in NLTE. Short *et al.* (1999) contains details of the sources of atomic data and the formulae for various atomic processes.

Table 2.1 shows which species have been treated in NLTE in the modeling presented here, and

Table 2.2: Levels of modeling realism.

Degree of NLTE	Model designation
None	LTE
Light metals only (H-Ca)	NLTE <sub>Light</sub>
Light metals & Fe	NLTE <sub>Fe</sub>

how many  $E$  levels and  $b - b$  (bound-bound) transitions are included in SE for each species.  $E$  is defined as the energy of the state with respect to the ground state of that ionization stage. Table 2.2 explains which elements are included in the degrees of realism modelled. I use the factor  $\log gf$ , where  $g$  is the statistical weight of the lower level and  $f$  is the oscillator strength of the transition to determine the intrinsic strength of the line, and is read in from the line lists used by PHOENIX. This factor is also used to determine how elements are treated in NLTE. Only levels connected by transitions of  $\log gf$  value greater than -3 (designated primary transitions) are included directly in the SE rate equations. All other transitions of that species (designated secondary transitions) are calculated with occupation numbers set equal to the Boltzmann distribution value with excitation temperature equal to the local kinetic temperature, multiplied by the ground state NLTE departure co-efficient for the next higher ionization stage. I have only included in the NLTE treatment those ionization stages that are non-negligibly populated at some depth in the star's atmosphere. As a result, I only include the first one to four ionization stages for most elements. Additionally, tens of millions of transitions are included with the approximate treatment of LTE.

NLTE effects can depend sensitively on the adopted values of atomic parameters that affect the rate of collisional and radiative processes. Atomic data for the energy levels and b-b transitions have been taken from Kurucz (1994) and Kurucz & Bell (1995). We have used the resonance-averaged Opacity Project (Seaton *et al.*, 1994) data of Bautista *et al.* (1998) for the ground-state photo-ionization cross sections of Li I-II, C I-IV, N I-VI, O I-VI, Ne I, Na I-VI, Al I-VI, Si I-VI, S I-VI, Ca I-VII, and Fe I-VI. For the ground states of all stages of P and Ti and for the excited states of all species, we have used the cross sectional data previously incorporated into PHOENIX, which are from Reilman & Manson (1979) or those compiled by Mathisen (1984). We account for

---

coupling among *all* bound levels by electronic collisions using cross sections calculated with the formula of Allen (1973). We do not use the formula of Van Regemorter (1962) for pairs of levels that are connected by a permitted transition because we have found that doing so leads to rates for transitions within one species that are very discrepant with each other, and this leads to spurious results. The cross sections of ionizing collisions with electrons are calculated with the formula of Drawin (1961).

For my models, I calculated intensity grids covering the region 1000 Å to 4000 Å with  $\Delta\lambda = 0.02$  Å, giving a resolution of  $R = \lambda/\Delta\lambda = 150000$ .

## 2.3 The Atmospheric Integrator

The code developed for this work allows an integrated flux spectrum to be produced for a star with non-uniform surface parameters. The intensity grid results are convolved with the instrumental profile of the OAO-2 satellite. Each spectrometer has a response function covering about 40 Å, so this convolution smoothes over the individual lines. The resulting spectrum, with  $\Delta\lambda = 0.02$  Å, is significantly oversampled, so I re-sample the convolved intensity files to a more realistic sampling of  $\Delta\lambda = 10$  Å. At this resolution, the individual lines are not visible, and the bins are large enough that the effects of the Doppler shift are not significant. The OAO-2 instrument profile is given in Table 2.3. Spectrometer 1 covers the wavelength range 1850 to 3600 Å and spectrometer 2 covers the wavelength range 1160 to 1850 Å. I fitted these profiles piecewise to produce a function defined over the entire region, allowing me to convolve the profile with the intensity files produced by PHOENIX. These fits are shown shown in Figs. 2.1 and 2.2. The convolution was tested by convolving a field of uniform intensity to ensure that the area under the curve was conserved during this process.

The input to the integration code comes from stellar evolution models generated by ROTORC. These models were evolved to match the observed temperature and luminosity of Achernar, but have varying degrees of oblateness. Details of the evolution of these models is described in Chapter

Table 2.3: The profile of the OAO-2 spectrometers, as given by Code &amp; Meade (1979).

$I/I_c$	$\Delta\lambda(\text{\AA})$	
	Spec. 1	Spec. 2
0.9	10.3	5.5
0.8	13.2	7.9
0.7	16.9	9.3
0.6	19.1	10.8
0.5	22.0	12.0
0.4	24.2	14.5
0.3	27.1	19.0
0.2	31.	28.5
0.1	36.	40.
0.05	48.	50.

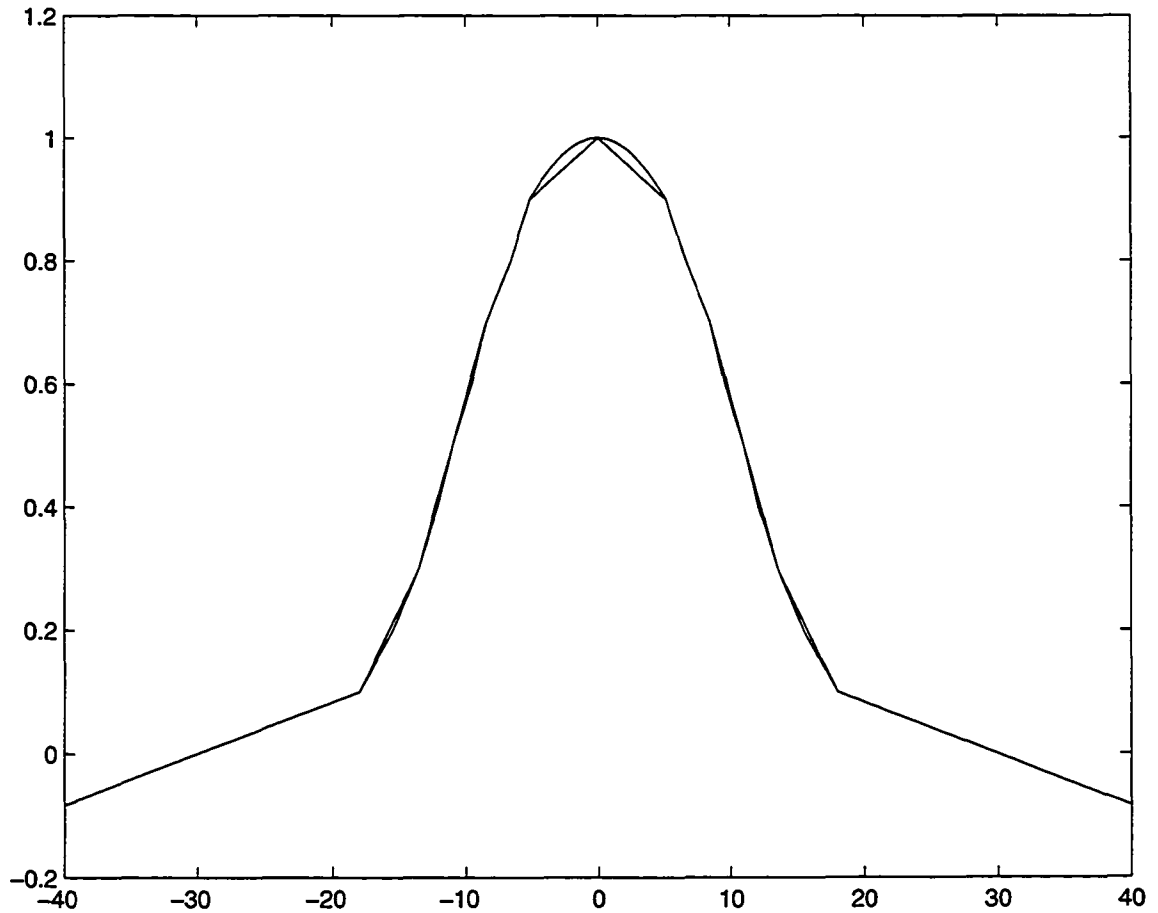


Figure 2.1: Fits to the instrumental profiles for spectrometer 1. The resulting fit gave a piecewise function used to convolve the PHOENIX intensity files.

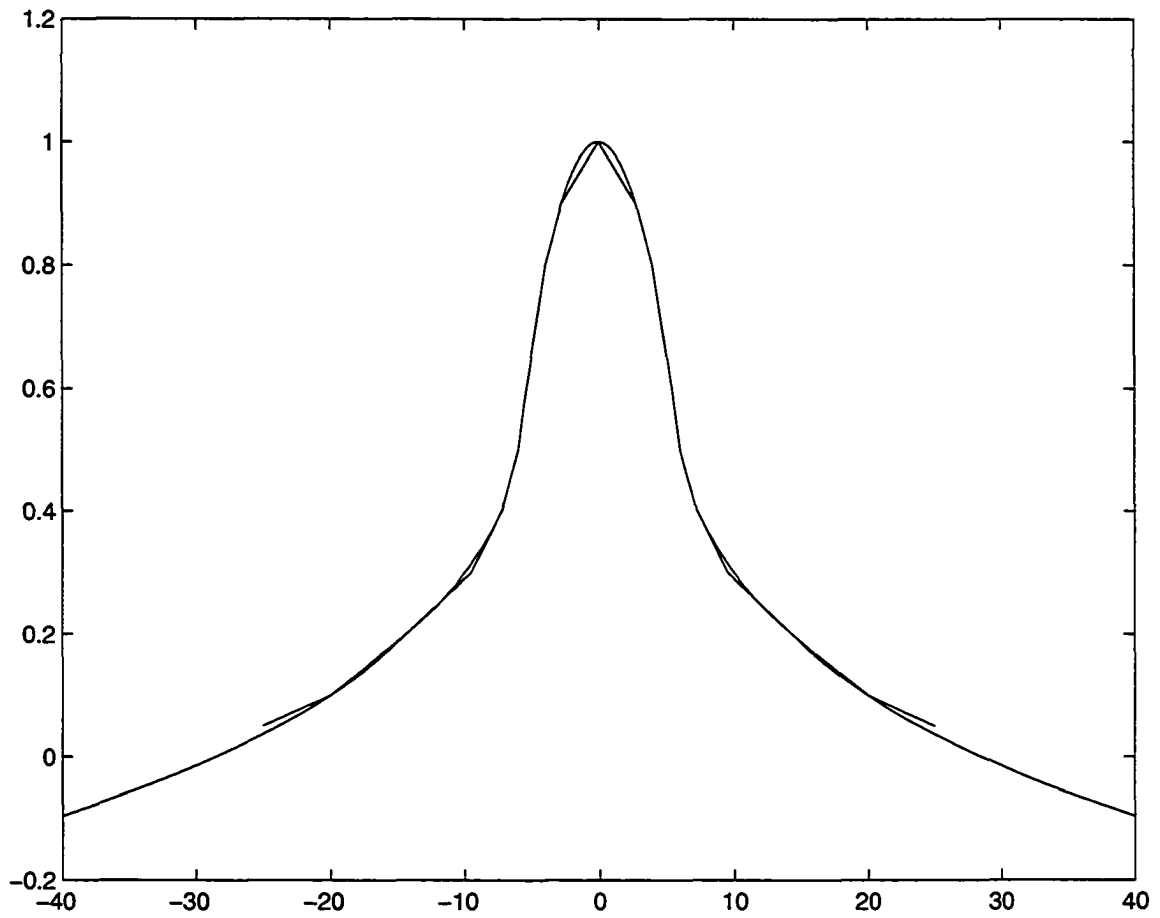


Figure 2.2: Same as for Fig. 2.1 for spectrometer 2.

3. From these models, I was able to generate effective temperatures and gravities as a function of latitude. These values determined the required range of model atmospheres produced by PHOENIX. I used a grid with temperature range of 11000 to 25000K with 2000K spacing and a range in  $\log g$  of 2.3 to 3.9, with spacing of 0.2. To generate the synthetic SEDs, I then interpolated within this grid to calculate the flux from each point on the surface of the star.

For each wavelength, I wish to evaluate the integral

$$F_{\lambda}(i) = \int_{\theta} \int_{\phi} I_{\lambda}(\xi(\theta, \phi, i)) \frac{dA_{proj} \cos \xi(\theta, \phi, i)}{d^2} \quad (2.29)$$

where  $\theta$  and  $\phi$  are as previously defined and  $\xi$  is the angle between the local normal and the direction to the observer. This integral gives the observed flux from the star, taking into account the variation in surface temperature and gravity as well as the inclination of the rotation axis with respect to the observer.

To do this integration, the surface parameters (temperature, effective gravity, and radius) are read in or calculated from the output of ROTORC. The surface of the star is divided into a mesh, typically 200  $\theta$  zones and 400  $\phi$  zones. This mesh spacing gives good spatial resolution over the surface of the star, as shown in Fig. 2.3. For each zone, the effective temperature and surface gravity are determined from the ROTORC model. The atmospheric integration code reads in the appropriate intensities from a grid of models in T and  $\log g$  produced by PHOENIX and performs logarithmic interpolation to determine the intensity produced by each zone on the surface of the star.

Next, the angle between the local surface normal and the line of sight to the observer ( $\xi$ ) is determined as follows. The model is axisymmetric, so the observer can be assumed to be directly above the prime meridian ( $\phi = 0$ ) of the star with no loss of generality. This gives the vector coordinates from the prime meridian towards the observer of  $\delta x = \sin i$ ,  $\delta y = 0$  and  $\delta z = \cos i$ .

To find the surface normal, I refer to Fig. 2.4. Starting with the radius at a given point on the model surface, R, extend this vector an arbitrary distance X. Next, extend the surface normal until

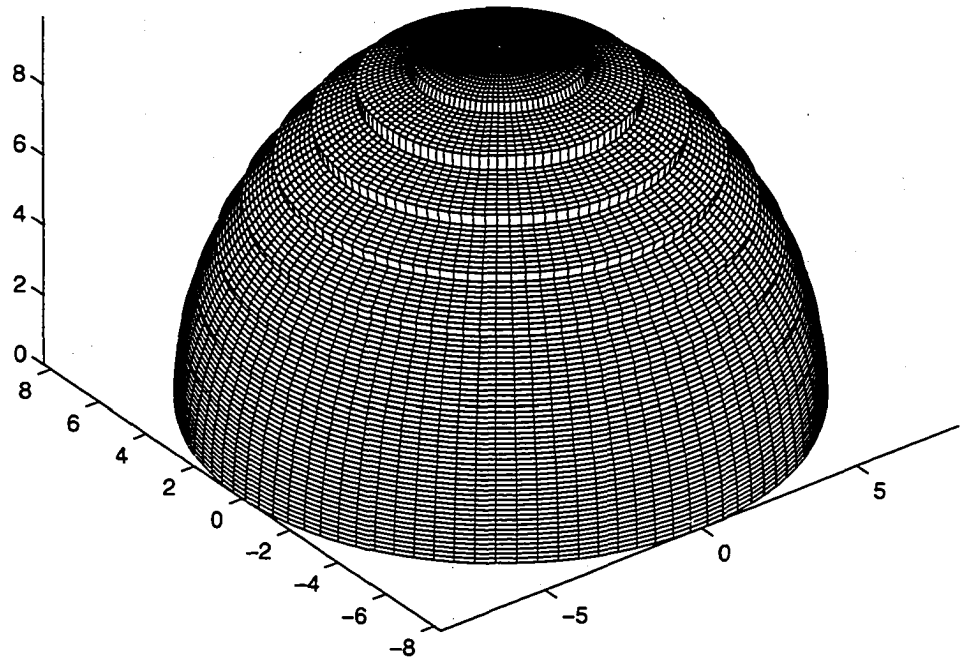


Figure 2.3: The integration mesh, shown over the upper hemisphere of the model. This mesh gives high spatial resolution over the surface of the star, increasing the accuracy of the integration.

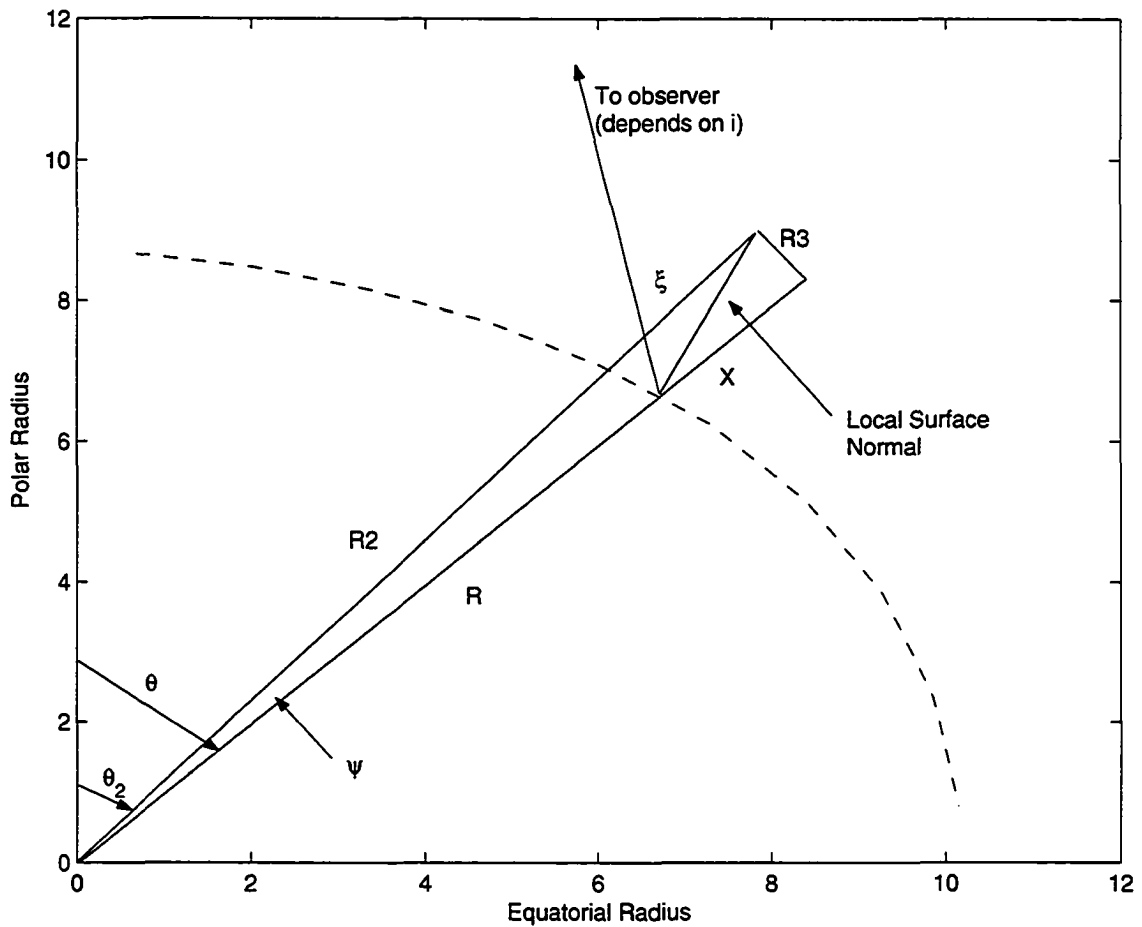


Figure 2.4: Geometry required to determine the normal to the surface. The distance from the model centre to the surface at the location of interest is  $R$ . This vector is extended by an arbitrary length  $X$ .  $R3$  is perpendicular to  $X$  and is bounded by the vector  $X$  and the surface normal. The vector  $R2$  runs from the model centre to the intersection of  $R3$  with the surface normal. Note that the vector in the direction of the observer could have a component outside the plane of the image.

it meets a vector  $R_3$ , perpendicular to  $X$ . The intersection of  $R_3$  and the surface normal occurs a distance  $R_2$  from the centre of the model. If  $R$  has a polar angle  $\theta$  and  $R_2$  has a polar angle  $\theta_2$ , then

$$\theta_2 = \theta - \psi \quad (2.30)$$

where  $\psi$  is positive in the northern hemisphere and negative in the southern hemisphere as a result of the oblate shape of the model. The angle,  $\Lambda$ , between the radial vector ( $X$ ) and the surface normal can be approximated by

$$\tan(\Lambda) \approx \frac{\delta R(\theta)}{R\delta\theta} \quad (2.31)$$

where  $\delta R$  is the the variation of the surface radius over an angle  $\delta\theta$ .

The vector normal to the surface can be defined by the spherical coordinates  $(R, \theta, \phi)$  and  $(R_2, \theta_2, \phi)$ , of which  $R$ ,  $\theta, \phi$  and  $\Lambda$  are known and  $X$  is assumed. From these, I can calculate

$$R_3 = X \tan \Lambda \quad (2.32)$$

$$R_2^2 = (R + X)^2 + R_3^2 \quad (2.33)$$

$$\psi = \arcsin\left(\frac{R_3}{R_2}\right). \quad (2.34)$$

This allows me to calculate the direction cosine between the surface normal and the vector pointing towards the observer,  $\xi$ . By definition the surface is not visible to the observer if  $\cos\xi < 0$ .

Once  $\cos\xi$  has been determined, an interpolation over the angles in the intensity files is performed. This gives the contribution to the total flux at a given wavelength from each grid zone. This flux is

then weighted according to the projected surface area for each mesh zone

$$dA_{proj} = R(\theta)^2 \sin\theta \cos\xi \sqrt{1 + \left(\frac{dR}{d\theta}\right)^2} \frac{1}{R^2} d\theta d\phi. \quad (2.35)$$

Which is the area for a spherical surface element with the local value of  $R$  times a correction factor to account for the distortion of the surface. I calculate the flux to be comparable to that observed at the Earth's surface. PHOENIX calculates the flux emitted at the surface of the star, so my flux must be scaled by  $1/d^2$  for comparison with the PHOENIX output.

The process is then repeated for each wavelength. For the synthetic SEDs discussed in this thesis, I calculated the flux at  $10 \text{ \AA}$  intervals for wavelengths covered by the OAO-2 spectrometers, 1160 to  $3600 \text{ \AA}$ . This allows for direct comparison with the UV spectrum taken by the OAO-2 satellite. However, this is not a limitation on the code, and any wavelength range or spacing could be used.

To ensure that the integrator is working correctly and that  $\cos\xi$  was calculated correctly, I confirmed that the SED of a spherical star was invariant with respect to inclination. I found that the inclination had no effect on the resulting spectrum. Also, for asymmetrical stars, the SED produced at an inclination of  $0^\circ$  was identical to that produced at an inclination of  $180^\circ$ . To test the output of the integrator, I compared the final *flux* spectrum for a uniform sphere produced by PHOENIX and by my atmospheric integrator. PHOENIX performs the integration by adding up the contributions of a series of concentric annuli (Mihalas, 1978, pp 11-12), while my integrator uses a mesh in  $\theta$  and  $\phi$ . The two flux spectra are very similar overall, although there are some slight variations. These variations are thought to be slight numerical differences resulting from the methods of integration. The differences over a small wavelength region can be seen in Fig. 2.3. Another difference between these two models is the order of operations. In my model, I convolve the  $0.02 \text{ \AA}$  spaced intensity grid and then integrate the product. In the PHOENIX model, the SED is calculated at  $0.02 \text{ \AA}$  and then convolved. I checked that these two operations commute by running a small section of the intensity grid at  $0.02 \text{ \AA}$  and then comparing it to the PHOENIX flux spectrum. On average, the two

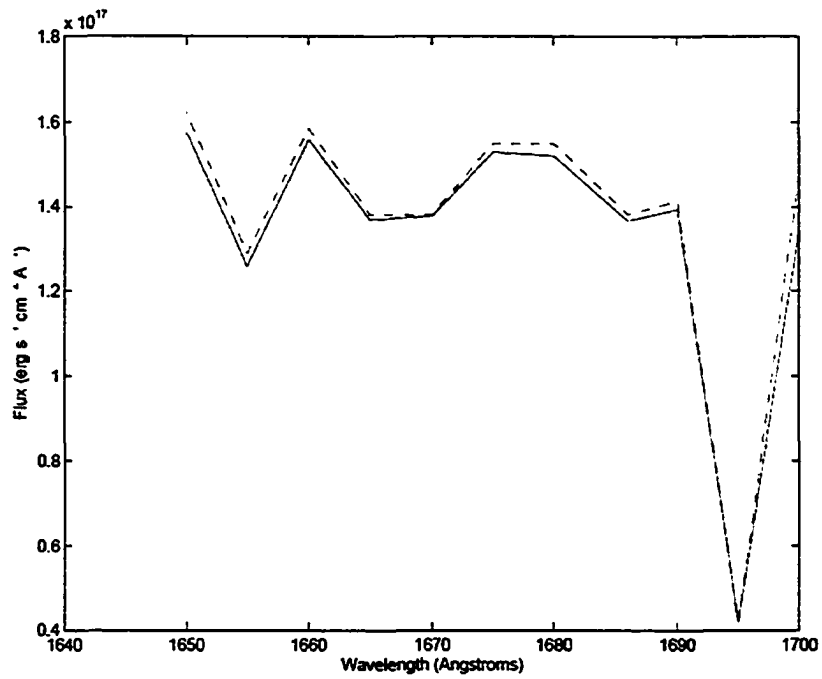


Figure 2.5: Comparison between the integrated and convolved spectra produced by PHOENIX (dashed) and the code developed for this thesis (solid). The PHOENIX spectrum is integrated at 0.02 Å spacing and then convolved with the OAO-2 instrumental profile, while my integration convolves and then integrates on a 10 Å spacing.

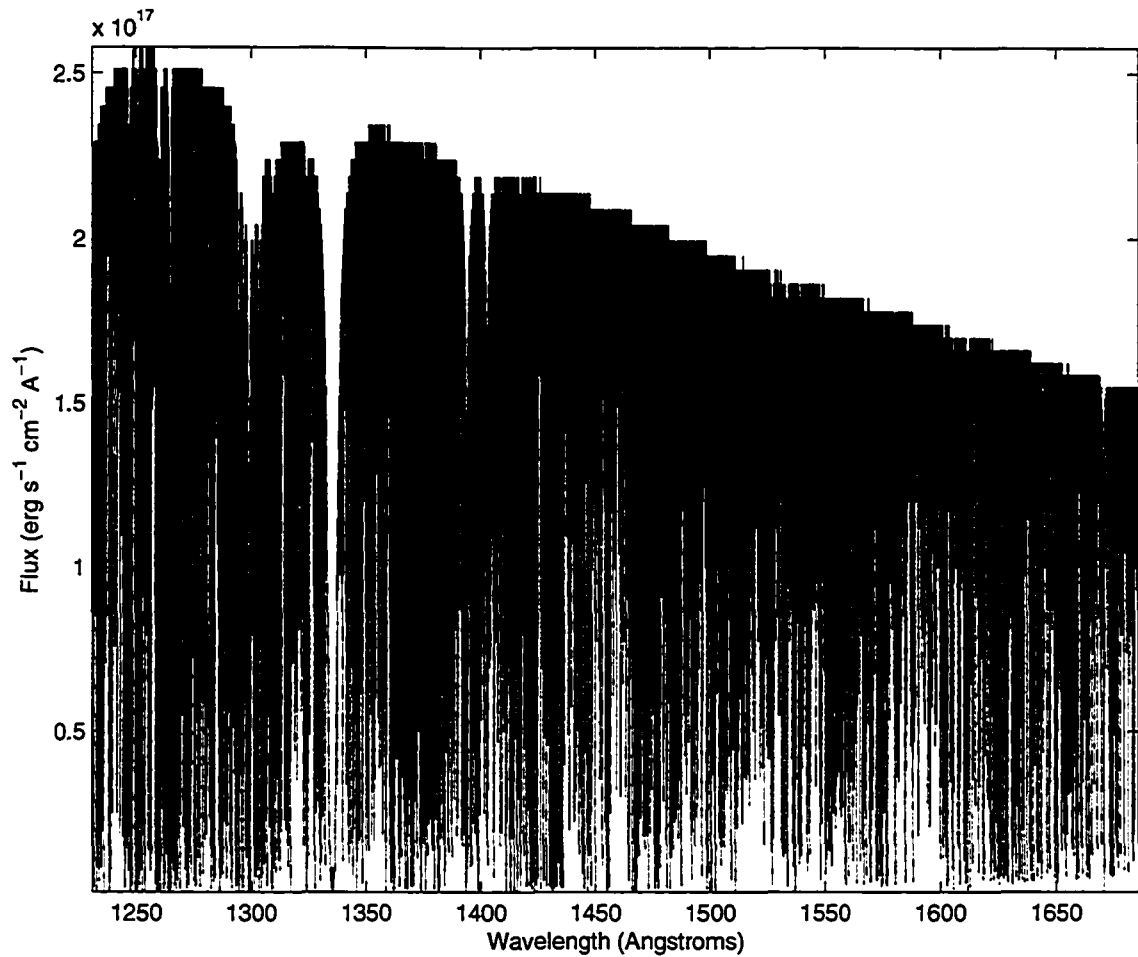


Figure 2.6: Comparison of unconvolved output of the atmospheric integrator and the SED produced by PHOENIX. The difference indicates that the integration and the convolution do not commute perfectly. However, the difference is small.

unconvolved spectra differ by about 4% over a region spanning  $150 \text{ \AA}$ , which corresponds to a 1% error in the temperature. This is a small enough error to be considered acceptable. The difference is also decreased by the convolution with the instrumental profile. The results of this comparison are shown in Fig. 2.6.

I also tested the spacing of my grid. Initially, my models were spaced at intervals of 0.2 in  $\log g$  and 2000 K in temperature. In general, I found the difference between successive gravities is small, so I concluded the resolution in  $\log g$  is sufficient. To test the resolution in temperature, I used a spherical model with a uniform temperature of 12000 K. I then used my integrator to produce a SED

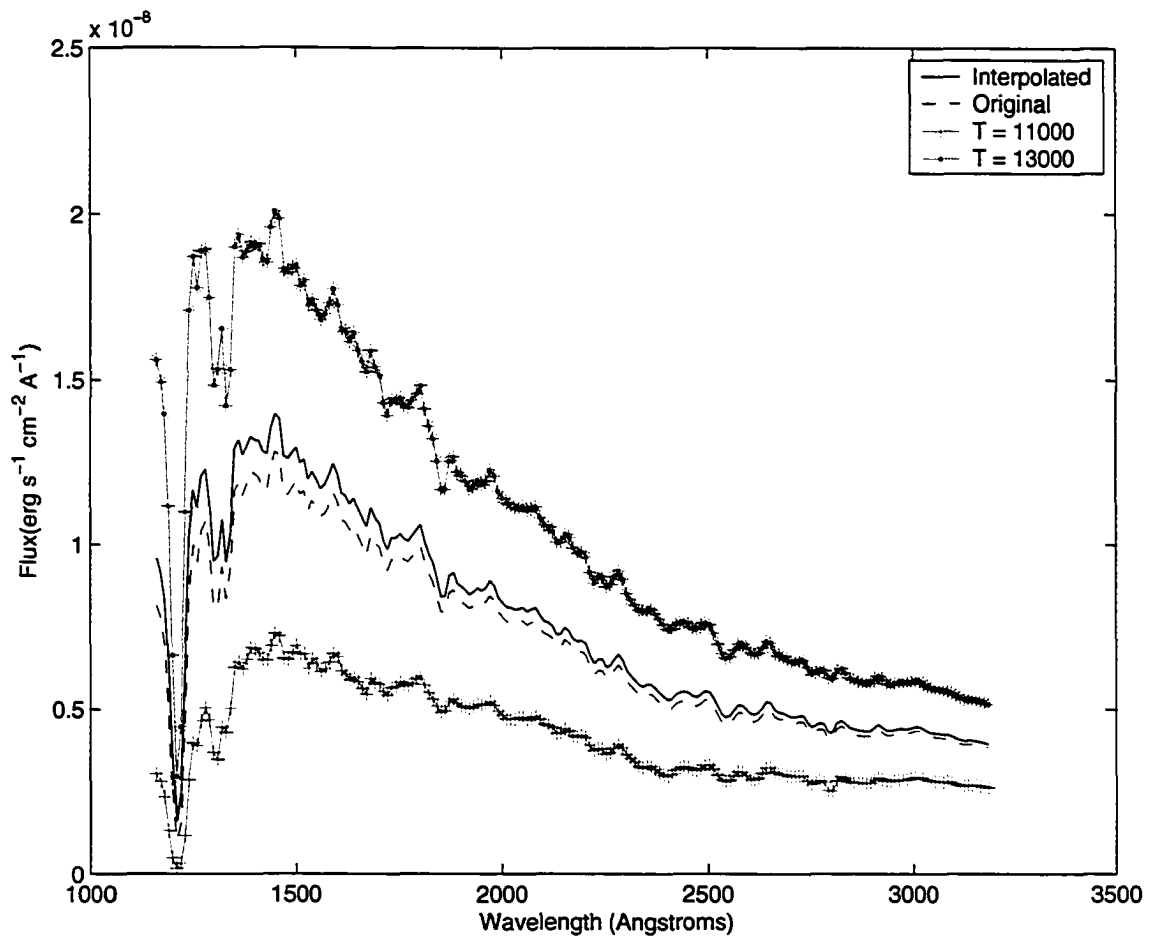


Figure 2.7: The results of the interpolation test. The solid line represents the interpolated spectrum at 12000 K, the dashed line represents the spectrum produced from the PHOENIX intensity file at 12000 K and the dash-dot lines are the spectra at 13000 and 11000 K.

for this model based on intensity files at 11000 and 13000 K. Next, I compared this to a SED for the same model based on the the intensity files at 12000 K (see Fig. 2.7). To estimate how accurate the interpolation is, I took the ratio of the two 12000 K models. The fourth root of this ratio gave me an estimate of the ratio of the temperatures corresponding to these fluxes. On average, the ratio calculated was 0.98, corresponding to a 2% error in the temperature. I concluded that this amount of error is acceptable, and hence the temperature spacing of 2000 K is sufficient.

# Chapter 3

## Structure Models

The general properties of Be stars vary widely from source to source. According to the Bright Star Catalogue, Achernar is classified as a B3Vpe star (Hoffleit, 1992). According to Carroll & Ostlie (1996), B3V stars have effective temperatures around 18700K, luminosities of  $1900L_{\odot}$ , and mass of  $7.6M_{\odot}$ . Using data for binary systems, Harmanec (1988) determined that B3 stars typically have temperatures of 19000K, but masses as low as  $6M_{\odot}$ . Jerzykiewicz & Molenda-Żakowicz (2000) used the Hipparcos data to derive empirical relationships for the luminosity and radius of a star based on observable properties of 32 stars. Measurements made by the Hipparcos (Perryman *et al.*, 1997) and OAO-2 satellites (Code & Meade, 1979), find that Achernar's properties are very different from those of a typical B3V star. Table 3.1 compares of the properties determined by various investigators, as well as the values adopted in this study.

One of the original goals of this project was to use rotating 2D models to constrain the internal angular momentum distribution of  $\alpha$  Eridani. The first step in this process was to rule out solid body rotation, verifying the conclusion reached by Domiciano de Souza *et al.* (2003). A star undergoing solid body rotation at critical velocity has a maximum axial ratio of  $a/b = 1.5$ . Observationally, most stars appear to lose mass from the polar regions rather than the equator, so they are generally assumed to be rotating below critical velocity. Domiciano de Souza *et al.* (2003) observed Achernar using optical interferometry and deduced an axial ratio of  $a/b = 1.56 \pm 0.05$ . This ratio indicates that solid body rotation is unlikely in this case, and based on their models, Achernar cannot be rotating as a solid body. The problem gets worse if inclination effects are taken into account. The observed axial ratio is 1.56, but this only reflects the true axial ratio if Achernar has an inclination of  $90^{\circ}$ . In all likelihood, the star is inclined, making the true axial ratio even larger, which implies

Table 3.1: Properties of Achernar compared to typical B3 stars. The first two entries in the table are typical values for B3 stars, all others refer specifically to Achernar.

$\log T_{eff}$	$\log L/L_{\odot}$	$M/M_{\odot}$	$R/R_{\odot}$	$\pi$ (")	Source
4.27	3.27	7.6	4.2	N/A	Carroll & Ostlie (1996) B3 stars
4.268	N/A	8.8	5.1	N/A	Harmanec (1988) B3 stars
4.162	3.520	6.2	9.1	N/A	Jerzykiewicz & Molenda-Żakowicz (2000) Achernar
4.162	3.44	N/A	8.3	0.025	Code <i>et al.</i> (1976) Achernar
N/A	N/A	N/A	N/A	0.023	Perryman <i>et al.</i> (1997) Achernar
4.30 <sup>a</sup>	N/A	6.07	12.0 <sup>b</sup>	0.023	Domiciano de Souza <i>et al.</i> (2003) Achernar
4.162	3.520	6-7.5	N/A	0.025	Adopted parameters

<sup>a</sup> Polar temperature

<sup>b</sup> Equatorial radius

Table 3.2: Properties of uniformly rotating models closest to Achernar.

Mass ( $M_{\odot}$ )	Z	$T_{eff}(K)$	L ( $L_{\odot}$ )	$v_{eq}$	$R_{eq}/R_p$
6.5	0.02	14523	3435	217 $\text{kms}^{-1}$	1.19
6.5	0.03	14507	3053	266 $\text{kms}^{-1}$	1.30
6.6	0.04	14520	3136	284 $\text{kms}^{-1}$	1.33

that the polar radius is even smaller than the estimate given in Domiciano de Souza *et al.* (2003). This is especially true when the  $v\sin i$  of Achernar is considered. At  $225 \text{ kms}^{-1}$ , Achernar has a much lower  $v\sin i$  than many B stars, so it is likely to have a significant inclination. This velocity is not high enough to produce the observed oblateness if it is the true equatorial velocity.

Our first model has a mass of  $7.5 M_{\odot}$  and metallicity of  $Z = 0.02$ . I included solid body (uniform) rotation on the ZAMS and evolved the model using local conservation of angular momentum. The mass of this model was chosen based on pre-existing 8 and  $5 M_{\odot}$  models. I interpolated the temperature and luminosity of these models to estimate the mass that would reach the temperature and luminosity of Achernar. I then tried to make ZAMS models with a variety of equatorial velocities. These models fail to converge if the ZAMS surface equatorial velocity is greater than  $545 \text{ km s}^{-1}$ . Of the models that converged, models that reach the location of Achernar in the HR diagram have ZAMS surface velocities of  $495 \text{ kms}^{-1}$  and  $510 \text{ kms}^{-1}$ , resulting in axial ratios  $a/b$  of  $\sim 1.23$  and  $1.27$  respectively, where the first model is viewed equator on ( $i = 90^{\circ}$ ) and the second is viewed at an inclination of  $70^{\circ}$  to match the observed  $v\sin i$ .

I also ran models with metallicity of  $Z = 0.03$  and  $Z = 0.04$ . These models all had masses of around  $6.5 M_{\odot}$ , in better agreement with the estimated mass of Achernar. With uniform rotation on the ZAMS, the best matches for these models are shown in Table 3.2. In this table, it appears that increasing metallicity results in increasing oblateness. This is deceiving, as one of the effects of increasing metallicity is to move the stars observed location in the HR diagram to the right. So, in Table 3.2, the more metal rich models reach the location of Achernar earlier in their main sequence evolution when their rotation is more rapid.

From these results, I concluded that although I could model Achernar as a main sequence star

near the end of core hydrogen burning, matching its observed temperature, luminosity and  $v \sin i$ , I could not match its observed oblateness using uniform rotation.

I varied the internal angular velocity distribution so that the angular velocity increases inwards. I did this by applying a simple power law down to a fractional radius of 0.001. I used a power law of the form

$$v = v_{surf,eq} \varpi^x \quad (3.1)$$

where  $x = 1$  gives solid body and  $\varpi$  is the distance perpendicular from the rotation axis; i.e.,  $\varpi = (r/R) \sin \theta$ . I studied values of  $x$  between 0.75 and 1. As  $x$  decreases, the models became increasingly difficult to converge, and the evolutionary tracks shift farther down and to the right in the HR diagram, requiring more massive models to match Achernar's luminosity and effective temperature. A  $6.6 M_{\odot}$  model with the power law given in Eqn. 3.1 and  $x = 0.6$  reaches the same temperature as Achernar at the end of core hydrogen burning, and is slightly less luminous. At this point, the ratio of equatorial radius to polar radius ( $R_{eq}/R_p$ ) = 1.33. Although these models were able to match the observed temperature, luminosity and  $v \sin i$  of Achernar, they still could not match the observed oblateness. However, the change in angular momentum distribution produced does move the oblateness in the right direction.

I tried a more complex power law, based on the form used by Jackson *et al.* (2004)

$$v = \frac{v_s(1 + \alpha^x)}{1 + (\alpha\varpi)^x} \quad (3.2)$$

where  $\varpi$  is defined as for equation 3.1,  $\alpha$  is a normalization constant and  $x$  is typically between 1 and 2. This required even more massive models. The angular momentum distributions produced by the different power laws are shown in Fig. 3.1. The model I studied most had a mass of  $7.0 M_{\odot}$ ,  $Z = 0.02$  and  $x = 1.4$ . When this model reaches the appropriate temperature, it is much more luminous than

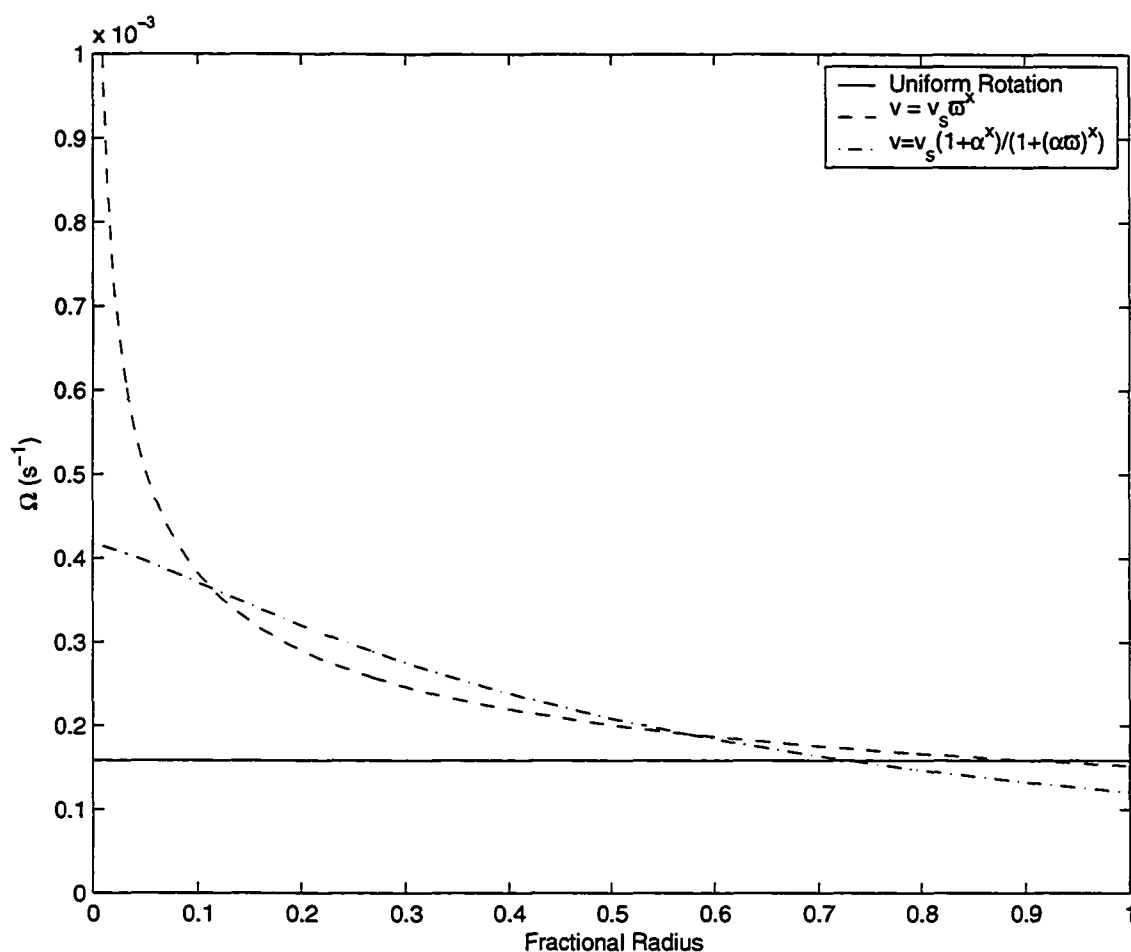


Figure 3.1: The distribution of angular momentum for the three power laws used: uniform rotation (solid), one described by Eqn. 3.1 (dashed) with  $x = 0.6$  and one described by Eqn. 3.2 with  $x = 1.4$ .

of Achernar. Although this model is not a good comparison to Achernar, it has other uses. This model crosses the track of the  $6.5 M_{\odot}$ ,  $Z = 0.02$  model at a temperature of approximately 16600 K and a luminosity of  $2500 L_{\odot}$ . The HR diagram showing the evolution sequences for these two models is shown in Fig. 3.2. This gives me two models with the same observed properties (temperature and luminosity), yet very different masses, radii and oblateness. This suggests that any differences that appear in the SEDs of these two models will be based on their mass and oblateness rather than their temperature and luminosity. These two models become very important in Chapter 4, where I study the effects of oblateness on the model SEDs.

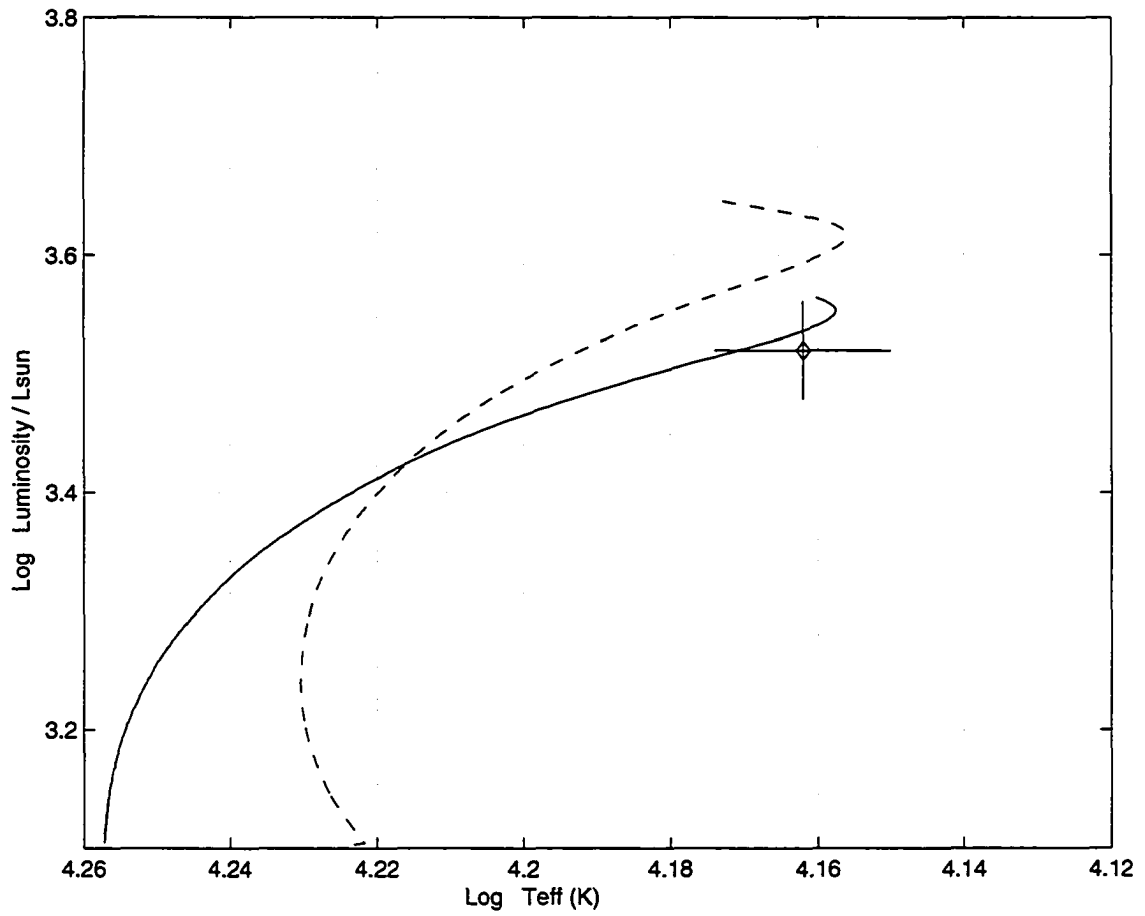


Figure 3.2: The evolution tracks of a  $6.5 M_{\odot}$  (solid) and a  $7.0 M_{\odot}$  (dashed) model. The observed location of Achernar is marked by a diamond.

Table 3.3: Properties of models closest to Achernar with different rotation laws.

Mass ( $M_{\odot}$ )	$T_{eff}$ (K)	$L$ ( $L_{\odot}$ )	$v_{eq}$	$R_{eq}/R_p$	Law
6.5	14523	3435	217 $\text{kms}^{-1}$	1.19	uniform
6.5	14514	2877 <sup>a</sup>	247 $\text{kms}^{-1}$	1.23	$x=0.6^b$
7.0	14520	3922 <sup>a</sup>	185 $\text{kms}^{-1}$	1.17	$x = 1.4^c$

<sup>a</sup> This model was chosen based on temperature only.

<sup>b</sup> Power law (see Eqn. 3.1)

<sup>c</sup> Power law (see Eqn. 3.2)

The properties of the models closest to the observed location of Achernar are summarized in Table 3.3. Again, the values in the table can be slightly misleading. Steeper power laws move the star down and to the right in the HR diagram, so more massive models are required to reach the same temperature and luminosity. Also, this means that the differentially rotating models reach the location of Achernar earlier in their main sequence evolution and have not slowed down as much as more uniformly rotating models.

By concentrating angular momentum towards the centre of the star, I was able to make the models much more oblate. On the early main sequence, these models can get as oblate as  $a/b = 1.46$ . However, as the model evolves along the main sequence, it expands and becomes more spherical. By the time it reaches the location of Achernar, its oblateness has dropped to  $a/b = 1.21$ . Even these more extreme models have not been able to reproduce the observed oblateness of Achernar. The evolution of the oblateness with age is shown in Fig. 3.3.

Models done by Jackson *et al.* (2004) using the self-consistent field (SCF) method were able to reproduce all of the properties of Achernar. They modeled chemically homogeneous stars with masses between  $6 \leq M \leq 15 M_{\odot}$ . These models were differentially rotating with the power law described in Eqn. 1.1. Their closest match was a  $9 M_{\odot}$  model with  $\alpha = 2.0$  and  $\eta (= \Omega_0/\Omega_{crit}) = 4.9$ . This model produced  $\log L = 3.51 L_{\odot}$ ,  $\langle T_{eff} \rangle = 14800$  K, and  $v_{eq} = 375 \text{ kms}^{-1}$ . Even this model is not a perfect match. The true oblateness ratio of this object is 3.45, but the  $v_{eq}$  implies an inclination of approximately  $37^{\circ}$ . However, as seen in Fig. 3.4, an inclination of  $49^{\circ}$  is required to match the observed oblateness. It should be noted that all of the models calculated by Jackson

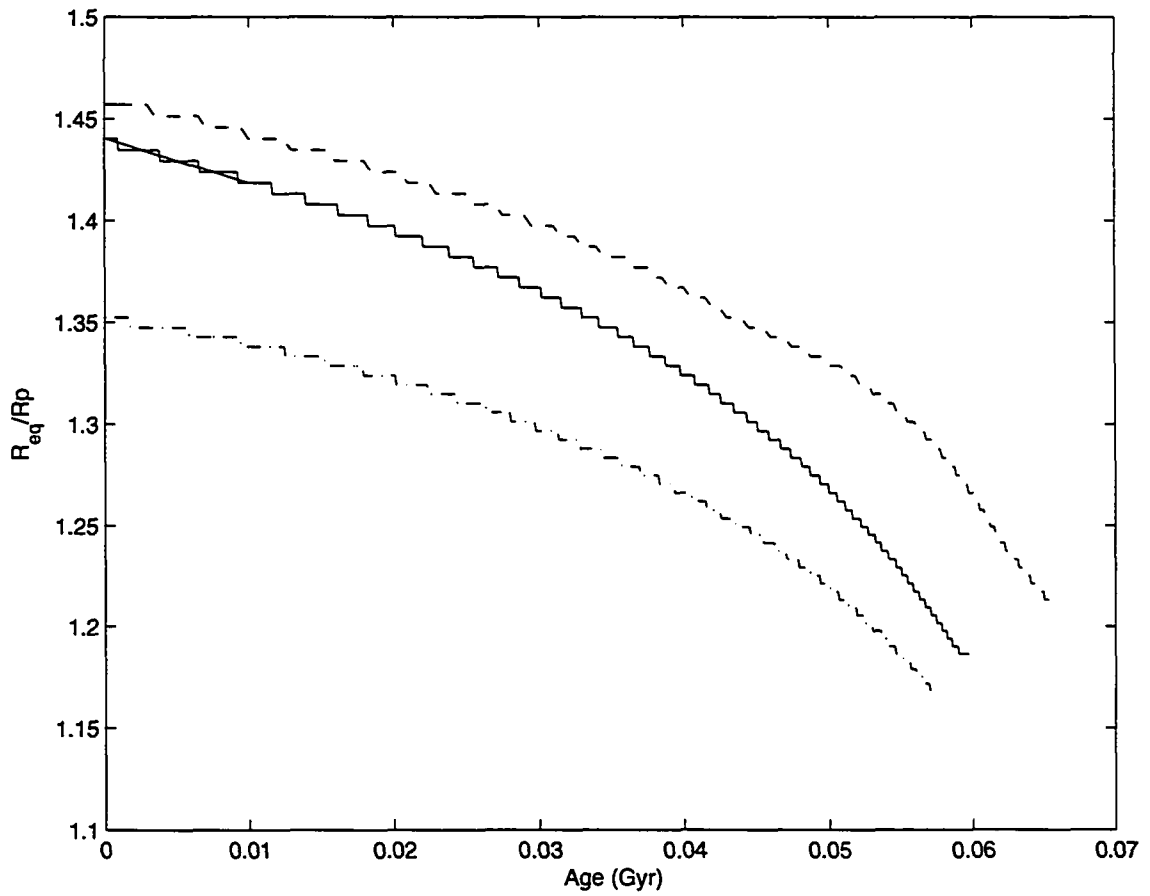


Figure 3.3: The evolution of the axial ratios for the three models. Solid -  $6.5 M_{\odot}$  model with uniform rotation on the ZAMS; Dashed - power law defined by Eqn. 3.1; Dot-dashed - power law defined by Eqn. 3.2. Although the stars are initially quite oblate, they become much closer to spherical with age.

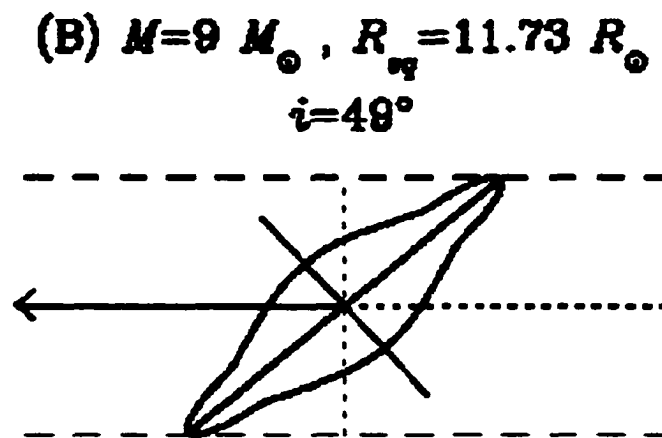


Figure 3.4: A cross sectional view of the photosphere of the SCF method model that most closely matches all the properties of Achernar. From Jackson *et al.* (2004), reproduced by permission of the AAS.

*et al.* (2004) are ZAMS models.

As described above, I tried to model the evolution of models using the same power law used by Jackson *et al.* (2004). My initial models used an exponent of  $x = 1.3$ , which moved the oblateness in the direction I needed in order to match the observations. I then decided to increase the exponent to see if I could reproduce the results of Jackson *et al.* (2004) and find a match to Achernar. I successfully produced models with an exponent of 1.4, although these models were too luminous and rotating too slowly to match the observations of Achernar. When the exponent was increased beyond this point, my models failed to converge. I believe this to be a result of the shape of the star. Referring back to Fig. 1.3, one can see that in some cases, the maximum radius of the star is not the equatorial radius. At present, ROTORC requires the largest radius to be at the equator. Although this is not the case for the successful match shown in Fig. 3.4, some of the less distorted models will have a bulge at mid-latitudes. ROTORC requires new models to be generated from old models in incremental steps. Some of the stages between models I can produce and the successful match have a bulge, and ROTORC is unable to reproduce these models. Although there should be no problem modelling the star shown in Fig. 3.4, the intermediate stages currently place it out of reach of ROTORC.

Another possibility that must be considered at this point is the accuracy of the original interferometric observations by Domiciano de Souza *et al.* (2003). The uncertainty in the measurements of the axial ratio is listed as  $1.56 \pm 0.05$ , which is quite small. Taking the Hipparcos distance of  $44.1 \pm 1.1$  pc, the polar and equatorial radius of Achernar can be found to an accuracy of less than  $0.5 R_{\odot}$ . However, this accuracy depends on several other factors. Interferometry actually measures the squared coherence factor ( $\mu^2$ ) of the starlight. This must then be calibrated against stable stars of known angular diameter. In this case, Domiciano de Souza *et al.* (2003) calibrated against three stars;  $\delta$  Phe,  $\chi$  Phe and  $\alpha$  PsA. The first two of these are K giants and have equivalent uniform disk diameters determined by spectrophotometry in the infrared (Cohen *et al.*, 1999). Different wavelengths probe different depths in the stellar atmosphere, so the angular diameter measured by

---

the VLTI team could be significantly different from that measured by Cohen *et al.* (1999). The third star was measured independently on the VLTI. Another problem with these measurements is the use of the uniform disk approximation. It is the uniform disk elliptical fit that gives the measured result of  $a/b = 1.56 \pm 0.05$ . As discussed later in this paper and by von Zeipel (1924) and Lovekin *et al.* (2005), gravity darkening in these hot stars can be important, particularly if there is significant differential rotation. This gravity darkening needs to be taken into account when determining the angular diameter. The presence or absence of a circumstellar disk and its effects on these observations has been discussed elsewhere in this thesis (see Chapter 1). Although there are many potential problems with these observations, for the purposes of this thesis, I have assumed the observations are correct. I have no reason to believe my models are more accurate, and find it more likely there is some aspect of the modelling I have omitted.

## Chapter 4

# The Intensity Spectra

Determining the metallicity of rapidly rotating stars is difficult. Even modest rotation velocities ( $v \sin i \sim 60 - 100 \text{ km s}^{-1}$ ) can be enough to blend the absorption lines (Daflon *et al.*, 2001). When the absorption lines are blended, measuring equivalent widths is difficult. In some cases, even identification of the individual absorption lines may be difficult as several lines can blend together to form a single spectral feature. Also, as the lines become broadened, the depth decreases, keeping the area under the curve constant. In extreme cases, the line may become so broad that the depth is within the uncertainty in the level of the continuum. This means I was unable to find a clear cut metallicity determination for Achernar, so I decided to test a variety of model atmospheres and see which one produced the best match to the observed spectrum.

I compared model atmospheres with all elements in local thermodynamic equilibrium (LTE) at metallicities of  $Z = 0.02$  (solar) and  $Z = 0.04$  (twice solar). The results are shown in Fig. 4.1. Note that Figs. 4.1 and 4.2 show only the peak of the UV spectrum so the scale is large enough to highlight the differences. The effects of line blanketing are greater in the  $Z = 0.04$  model. All of my flux calculations were calculated using Eqn. 2.29 to give the flux at the Earth's atmosphere. For a value of  $d$ , I have used 40.0 pc, corresponding to the distance used by Code *et al.* (1976). I compared the effects of model atmospheres with all elements in LTE to model atmospheres with light elements in non-LTE (NLTE) and the iron group elements in LTE. The result is shown in Fig. 4.2 (solid and dashed lines). Although some of the lines are more pronounced when light elements are in NLTE, there is little difference between the two spectra. Finally I studied the effect of including Fe in NLTE. This calculation included the first 4 ionization states for Fe. This comparison is also shown in Fig. 4.2 (dashed and dashed-dot lines). The effect of including the iron lines in NLTE is much

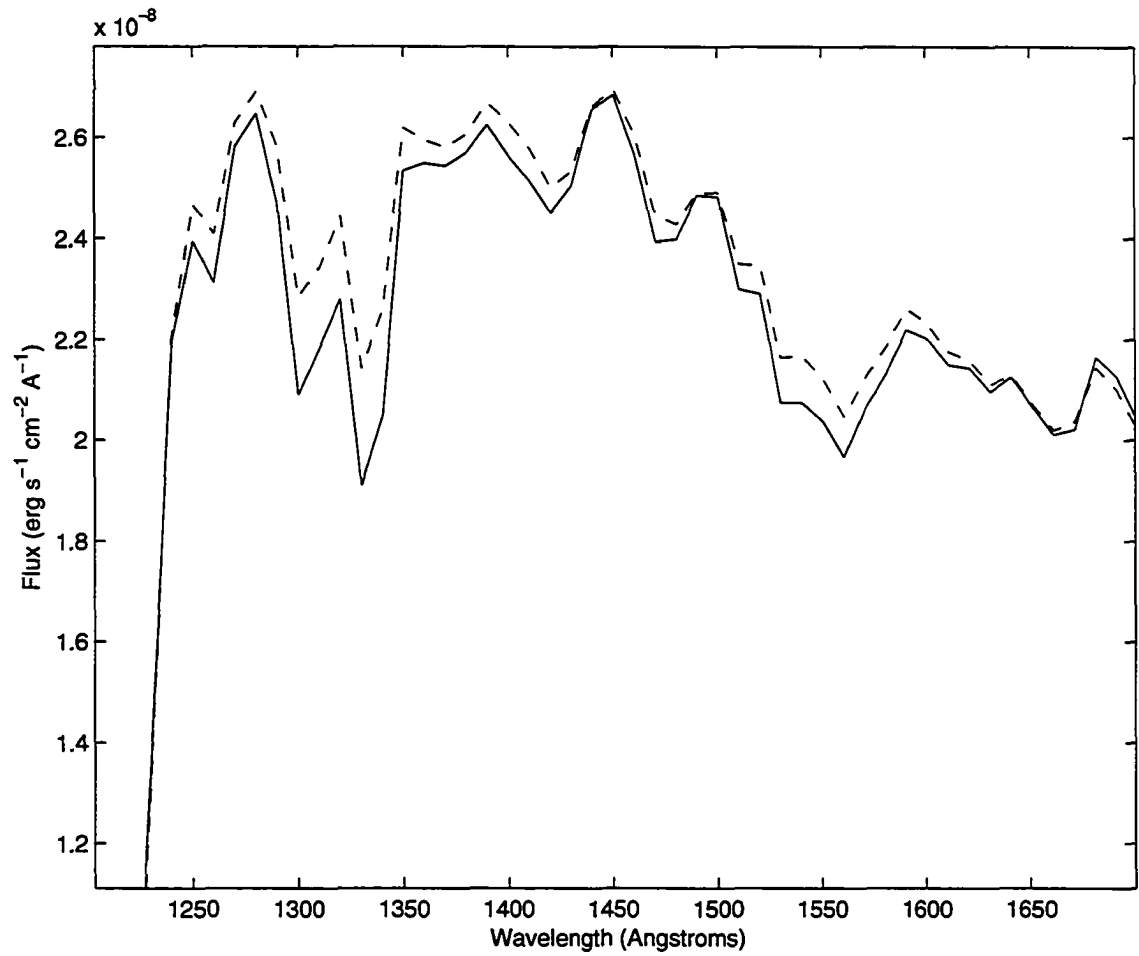


Figure 4.1: Comparison of LTE model atmospheres at  $Z = 0.04$  (solid) and  $Z = 0.02$  (dashed) for a uniform model with a temperature of 14000 K.

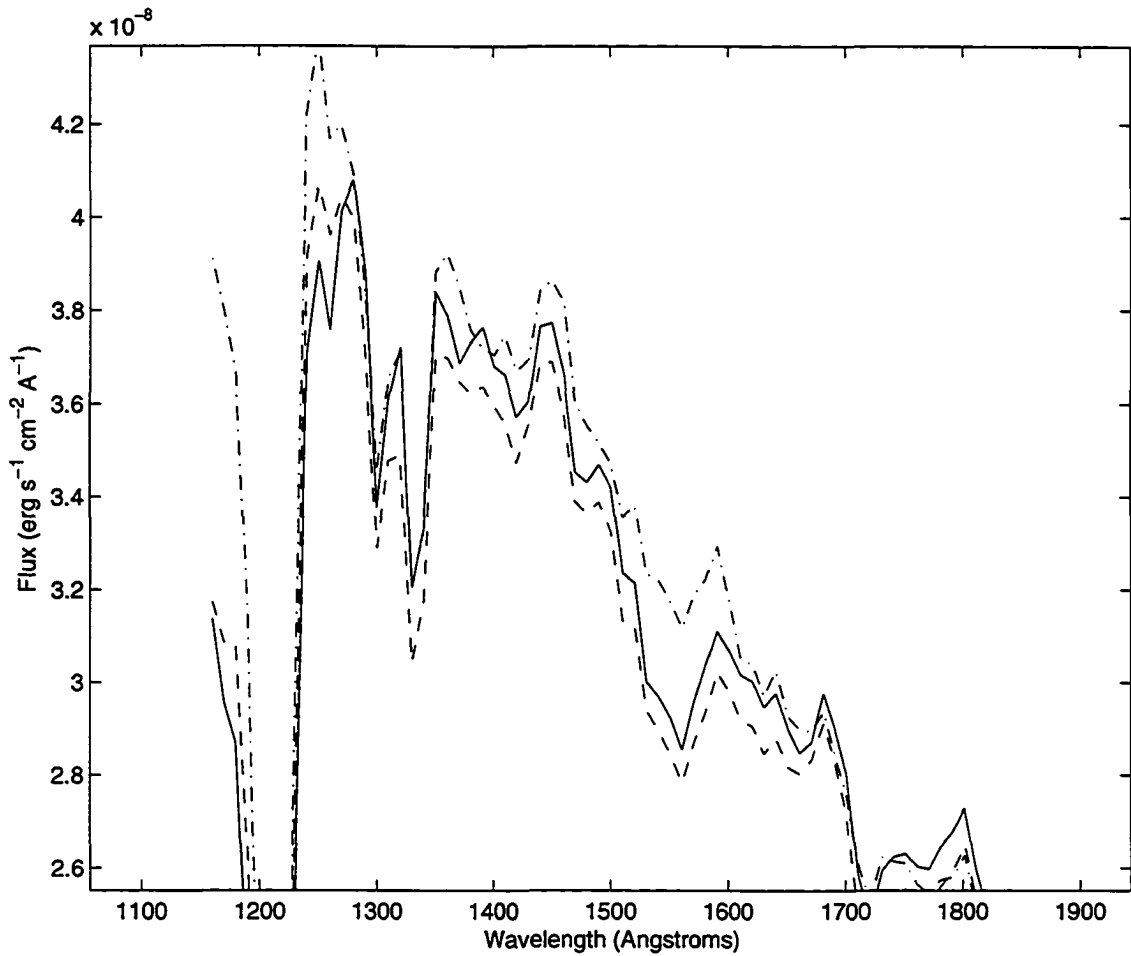


Figure 4.2: Synthetic intensity spectra generated using model atmospheres in LTE (solid line), with light elements in non-LTE (dashed line) and light elements and iron in non-LTE (dot-dashed line). The input model is a uniform spherical star with  $T_{eff}$  of 15000 K and a metallicity of  $Z = 0.02$ .

more pronounced than the effect of the lighter elements alone. I chose to include Fe lines in my non-LTE calculations partly to increase the realism of the model, but also because models with Fe in non-LTE more closely match the observed SED for Achernar.

Based on the above results, I found no reason to favour one particular metallicity based on the SEDs. However, I had other reasons for choosing to model Achernar using  $Z = 0.02$ . Although there is some evidence from atmospheric modelling for a much lower iron abundance for the sun, these values are based on very uncertain oscillator strengths (Kostik *et al.*, 1996). Instead, I have chosen to take the solar metallicity to be  $\sim 0.02$ , as required to match the helioseismology observations for

Table 4.1: Mean abundances of B stars (from Gies &amp; Lambert (1992) and Sofia &amp; Meyer (2001)) compared to solar abundances.

Element	B Stars <sup>a</sup> ( $\log \epsilon_X$ )	B stars <sup>b</sup> ( $\log(X/H)$ )	Sun <sup>c</sup> ( $\log \epsilon_X$ )
He	11.00	...	10.93
C	8.20	-3.77	8.39
N	7.81	-4.20	7.78
O	8.68	-3.41	8.66
Ne	7.97	...	7.84
Al	6.45	...	6.37
Si	7.58	-4.80	7.51
S	7.21	...	7.14
Fe	7.72	-4.42	7.45

<sup>a</sup> From Gies & Lambert (1992),  
excluding supergiants

<sup>b</sup> From Sofia & Meyer (2001)

<sup>c</sup> From Asplund *et al.* (2005)

a  $1 M_{\odot}$  model at the solar age (Antia & Basu, 2005; Bahcall *et al.*, 2005).

Several pieces of observational evidence favour a metallicity of approximately solar. Firstly, Achernar is close to the Sun ( $d = 44.1$  pc) (Perryman *et al.*, 1997), and hence its metallicity is likely close to solar. Another indication of the metallicity of Achernar comes from a study by Torres *et al.* (2000) which finds some evidence for a loose association of pre-main sequence stars centered around ER Eri. Although this association consists primarily of post-T Tauri stars, the age and location of Achernar is consistent with membership in this cluster. Observations of this cluster show it to be consistent with a metallicity of  $Z = 0.02$ . Finally, many studies of galactic B stars indicate their average metallicity is close to solar (Gehren *et al.*, 1985; Brown *et al.*, 1986; Lennon *et al.*, 1990) and there is no reason to suspect that Be stars are any different. Gehren *et al.* (1985); Brown *et al.* (1986) and Lennon *et al.* (1990) have studied the C, N and O abundances of main sequence B stars in the Galactic disk and found that these stars generally have a solar-like composition, regardless of distance from the Galactic centre. These results are confirmed by Gies & Lambert (1992), with a summary shown in Table 4.1. This is confirmed in a more recent study of OB associations by Daffon *et al.* (2001), showing that these stars have a metallicity slightly below solar, by about 0.1

to 0.3 dex. These determinations were made by spectrum synthesis using both LTE and non-LTE atmospheric models.

# Chapter 5

## Results and Discussion

For oblate stars, the inclination has a significant effect on the observed flux spectrum. A sample is shown in Figs. 5.1 and 5.2, which show the spectra for models inclined at 0, 30, 60 and 90 degrees. The spectra shown in Fig. 5.1 are based on an evolved  $6.5 M_{\odot}$  model with uniform rotation on the zero-age main sequence (ZAMS) and a surface equatorial velocity of  $v = 495 \text{ km s}^{-1}$ . This model has been evolved to the same evolutionary (i.e. ROTORC) effective temperature and luminosity as  $\alpha$  Eri, but with an oblateness of  $a/b = 1.19$  (see the first line of Table 3.3 for the full properties of this model.) Those in Fig. 5.2 are based on an evolved  $7 M_{\odot}$  model, rotating on the ZAMS with a power law of the form given in Eqn. 3.2. The ZAMS surface equatorial velocity of this model is  $v = 430 \text{ km s}^{-1}$ . This model has a similar evolutionary temperature and luminosity, but with an oblateness of  $a/b = 1.17$  (see the third line of Table 3.3 for the full details of this model.) It is important to note the differences in scale between Figs. 5.1 and 5.2. Although the results are similar, the difference between a pole on SED and an equator on SED is larger in the  $7 M_{\odot}$  model.

In the radiative regions of a star, flux is transported perpendicular to the equipotential surfaces. In an oblate star, the shape of the equipotentials directs much of the flux towards the polar regions. Since more energy is emitted from the polar regions of the star, the pole is correspondingly hotter. Since the polar region of these oblate models is hotter than the equator, the closer to pole on the star is observed, the more the polar region contributes to the observed flux and the higher the apparent effective temperature and luminosity of the star.

To determine the apparent effective temperature of the star, I considered several colour indices. I chose these indices based on SEDs produced from spherical models at uniform temperature. For each temperature and gravity, I created a structure model with radius of  $8.5 R_{\odot}$ , based on the

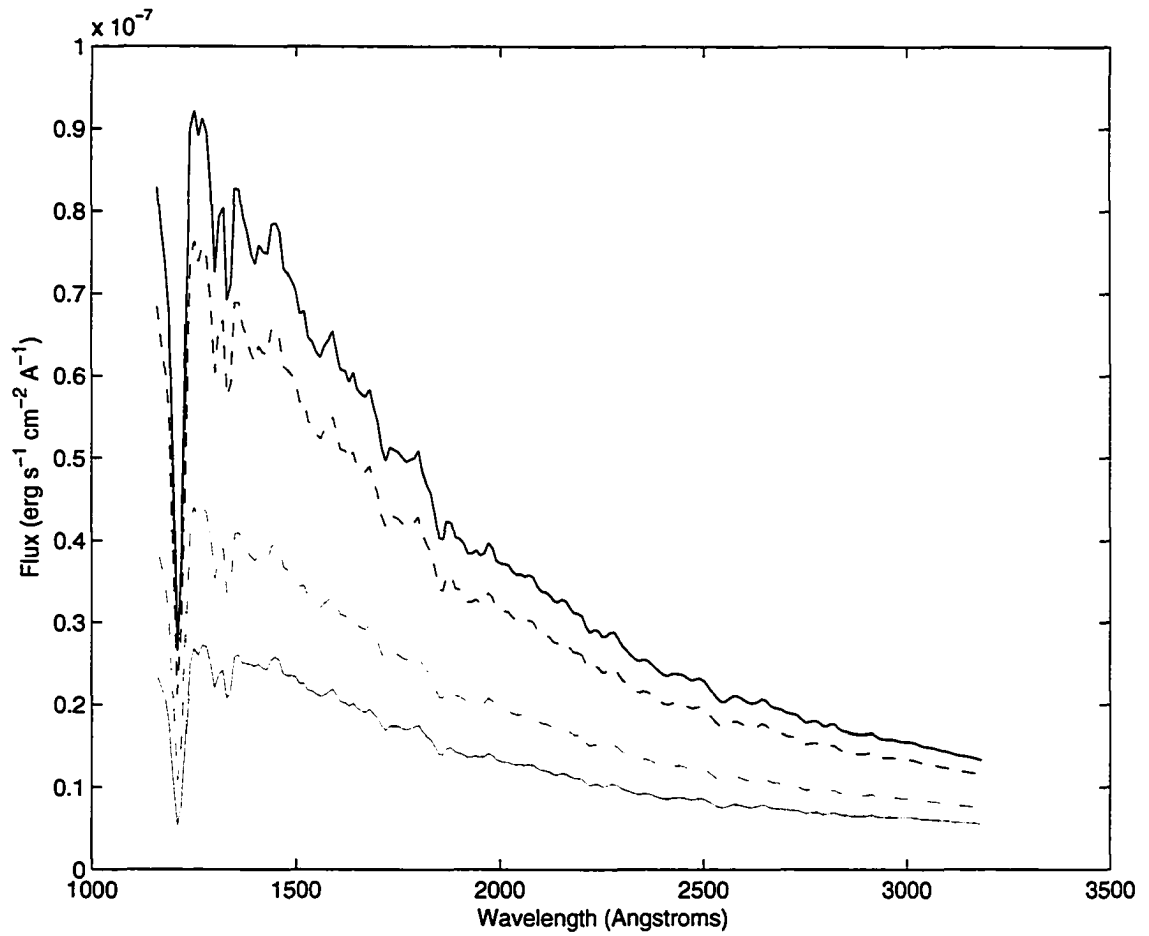


Figure 5.1: Synthetic flux spectra for a  $6.5 M_{\odot}$  model at inclinations of  $0^{\circ}$  (top solid)  $30^{\circ}$  (dashed)  $60^{\circ}$  (dot dashed) and  $90^{\circ}$  (lower solid).

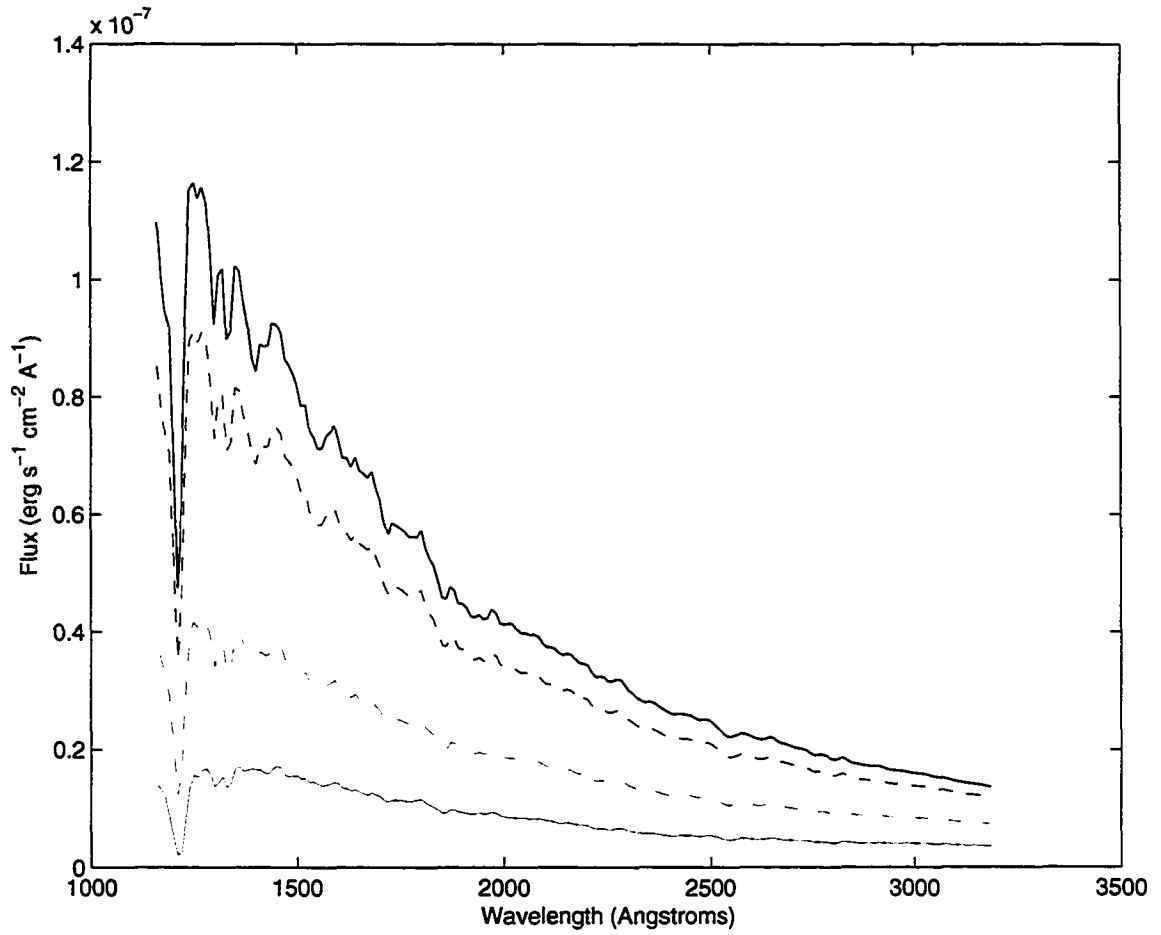


Figure 5.2: Synthetic flux spectra for a  $7 M_{\odot}$  model at inclinations of  $0^{\circ}$  (top solid)  $30^{\circ}$  (dashed)  $60^{\circ}$  (dot dashed) and  $90^{\circ}$  (lower solid).

measurements of Hanbury Brown *et al.* (1974). I then integrated over the surface of this model to produce a SED. In subsequent discussion, I will refer to this as the SED from a spherical model. For these models, I found several features that seemed to show a strong temperature dependence and then summed the flux in each passband. The four passbands chosen were: A:  $1450 \pm 10 \text{ \AA}$ , B:  $1265 \pm 15 \text{ \AA}$ , C:  $3140 \pm 40 \text{ \AA}$  D:  $1920 \pm 20 \text{ \AA}$ . Using these passbands, I defined three colours: A-B, A-C and A-D. I also used a fourth colour, based on the depth of the Lyman  $\alpha$  line. One of the two points were chosen to be as close as possible to the bottom of the Ly  $\alpha$  line, while the other was chosen at a pseudo-continuum level. This colour was given by the ratio of the flux sampled at  $1210 \text{ \AA}$  to the flux sampled at  $1240 \text{ \AA}$ . For each model atmosphere in my grid, I calculated a SED based on a uniform spherical model, which I used to calibrate the colours. I then examined the trends of these indices with temperature. I found that the Ly  $\alpha$  index had the strongest correlation with temperature. Each index was calculated at each temperature and gravity, giving 3 points at each temperature in most cases. I averaged the Ly  $\alpha$  index at each temperature to eliminate gravity effects and then fit the data with a third order polynomial, shown in Fig. 5.3. I then calculated the Ly  $\alpha$  index for the oblate star synthetic spectra at each inclination and used this fit to calculate a temperature for that SED at each inclination.

As a check on these inferred temperatures, I also calculated fits to the colour-temperature data for the other three colour indices. The results were quite similar for all four indices, with a variation among indices of at most  $\pm 300 \text{ K}$ . The four indices are most consistent near the equator, but diverge slightly towards the pole. Although I looked for indices that depended predominantly on temperature, some gravitational influence is unavoidable. gravity. As described above, Ly  $\alpha$  has the strongest correlation with temperature, but there may be other effects I have missed.

In the spectra shown in Figs. 5.1 and 5.2, the inferred temperature difference between 0 and 90 degrees is between 2000 and 500 K, depending on the details of the model. This is illustrated in Fig. 5.4, which shows the inferred effective temperature as a function of inclination for the two models described above.

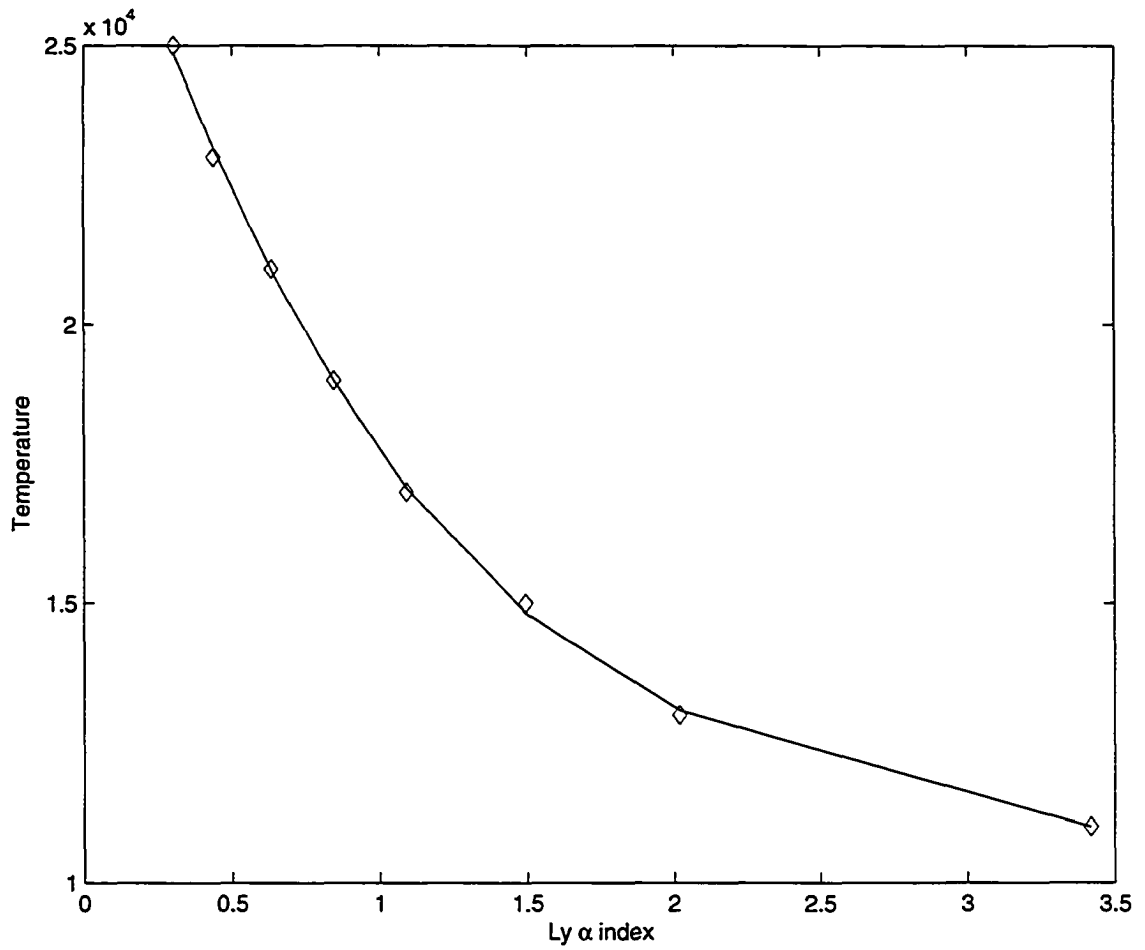


Figure 5.3: Polynomial fit to the averaged Ly  $\alpha$ -Temperature data. This fit was then used to calculate an inferred temperature for the synthetic SEDs.

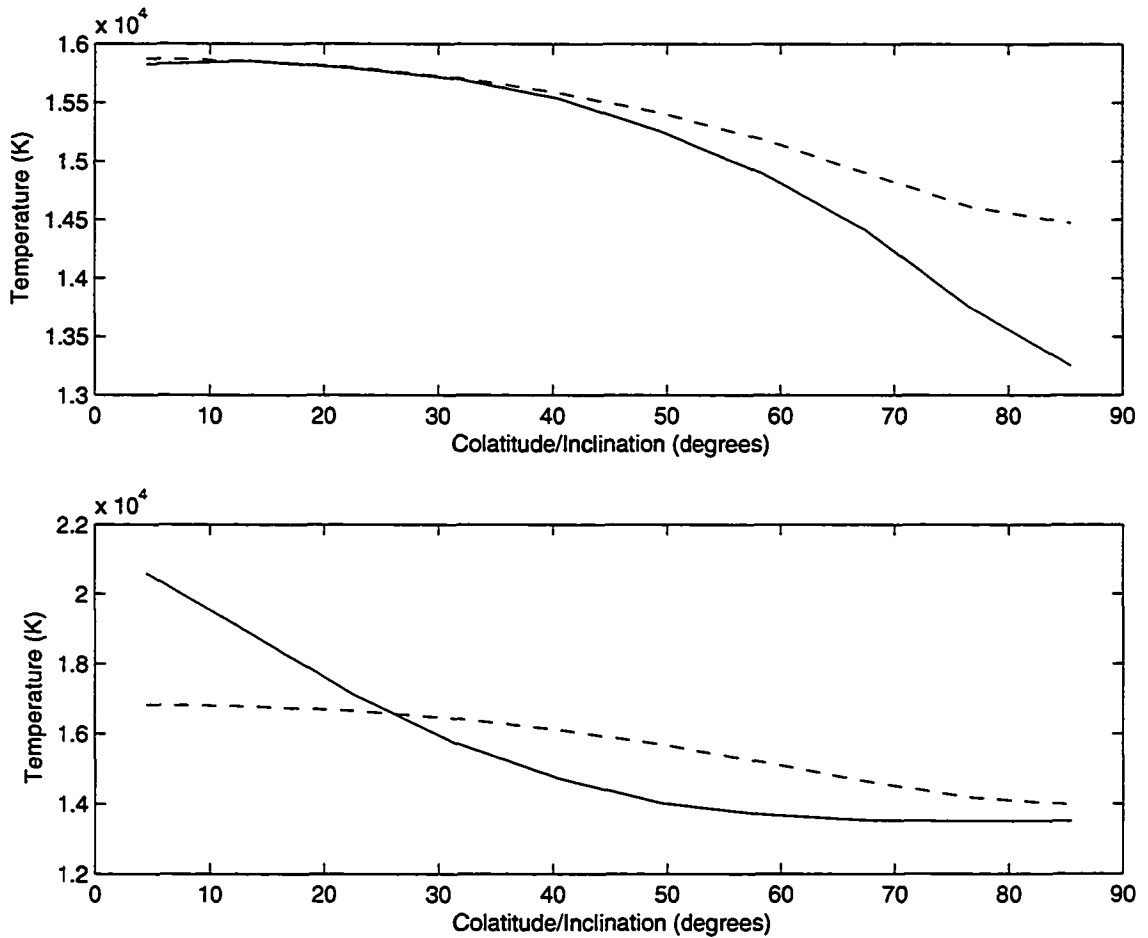


Figure 5.4: Top: The deduced effective temperature (dashed line) based on the synthetic SEDs as a function of inclination for the  $6.5 M_{\odot}$  model. The solid line shows the ROTORC effective temperature as a function of colatitude for the same model. The temperatures are evaluated at the midpoints of the  $\theta$  zones of the Bottom: Same as for top plot, but for the  $7 M_{\odot}$  model. Both models are evolved to approximately match the observed properties of Achernar.

ROTORC model.

Clearly, for more extreme angular momentum distributions, the temperature difference between the pole and the equator can become larger. The inferred effective temperatures for the two models discussed here range between 13000K and 18000K. The inclinations that best correspond to the evolutionary temperature of 14500K are approximately  $40^\circ$  for the  $7 M_\odot$  model and  $65^\circ$  for the  $6.5 M_\odot$  model. However, the inclinations required for the models surface velocity to reproduce the observed  $v \sin i$  are  $90^\circ$  and  $82^\circ$  respectively. The range of possible observationally determined temperature and luminosity over the full range of  $i$  for a given star is illustrated in Fig. 5.5. I calibrated the luminosity based on the same spherical models used to calibrate the colour indices. For each of these models, the radius and temperature are known, so the total luminosity is easily found from

$$L = 4\pi R^2 \sigma T^4. \quad (5.1)$$

Once I found the temperature for each synthetic SED, I performed linear interpolation between the spherical models to find the luminosity. The range of possible values is centered on the evolution track in this case, as my evolutionary temperature is effectively an average. However, for observed spectra, it could be very difficult to determine where on this curve the star actually lies.

Finally, I wished to see if there was any difference between the SEDs produced from very different structural models. In Fig. 5.6, I compare the SEDs of a  $6.5 M_\odot$  model and a  $7 M_\odot$  model, inclined at  $80^\circ$  and  $84^\circ$  respectively. This figure also shows the observed SED of Achernar seen by the OAO-2 satellite (Code *et al.*, 1976). The differences are highlighted in Fig. 5.7, which shows only the peak of the spectrum, where the differences are greatest. The underlying properties for the two models and Achernar are summarized in Table 5. The inclination of the  $6.5 M_\odot$  model SED was chosen to give a good match to the SED of Achernar at wavelengths beyond  $\sim 2500 \text{ \AA}$ . I then used linear interpolation to calculate the inclination of the  $7 M_\odot$  model that best fits the  $6.5 M_\odot$  model. These inclinations compare favourably with the inclinations required to match the observed  $v \sin i$  at  $90^\circ$

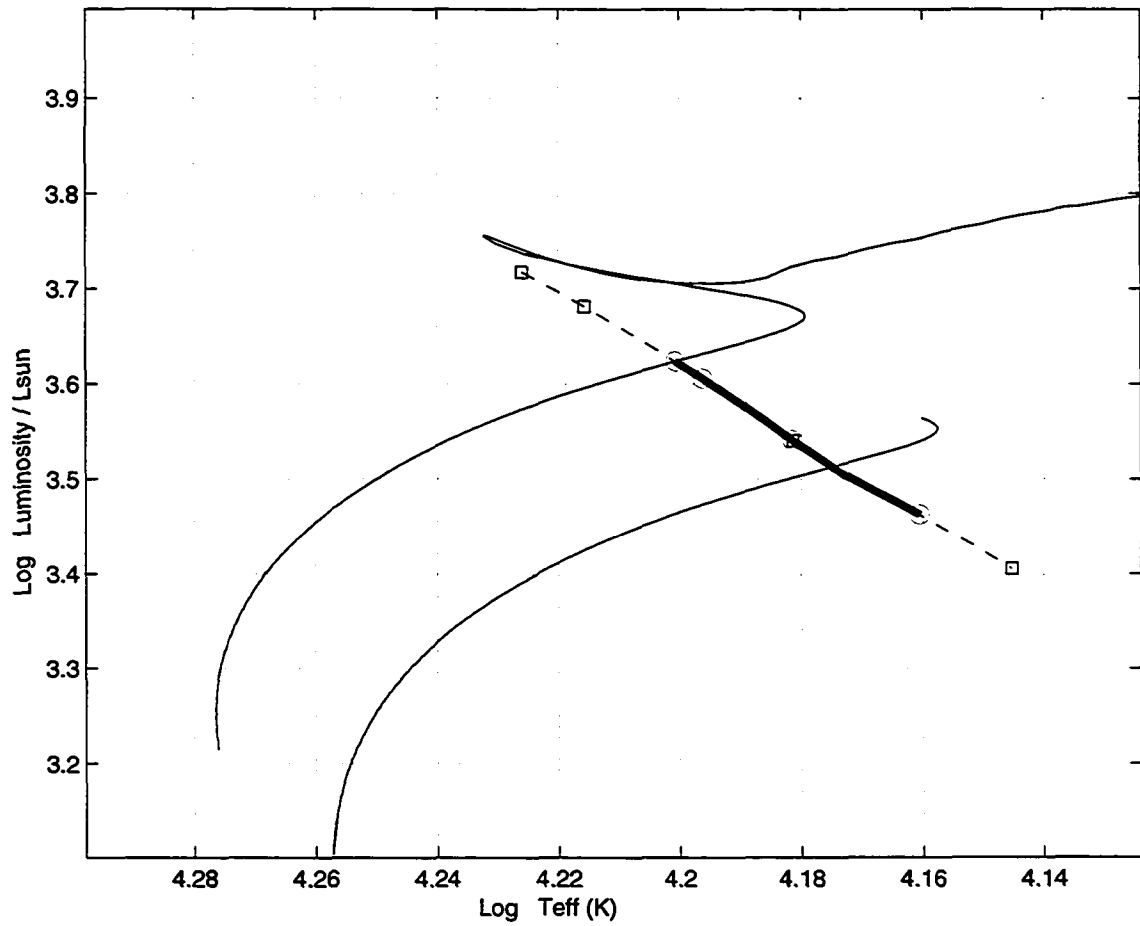


Figure 5.5: The possible temperature and luminosity ranges of my models. The bold line shows the values for the  $6.5 M_{\odot}$  model, while the dash line shows the values for the  $7.0 M_{\odot}$  model. The circles and square show, from left to right, where a star would be observed if inclined at  $0, 30, 60$  and  $90^{\circ}$  for the  $6.5$  and  $7 M_{\odot}$  models respectively. The evolutionary sequences for uniformly rotating  $7 M_{\odot}$  and  $6.5 M_{\odot}$  models are shown for comparison.

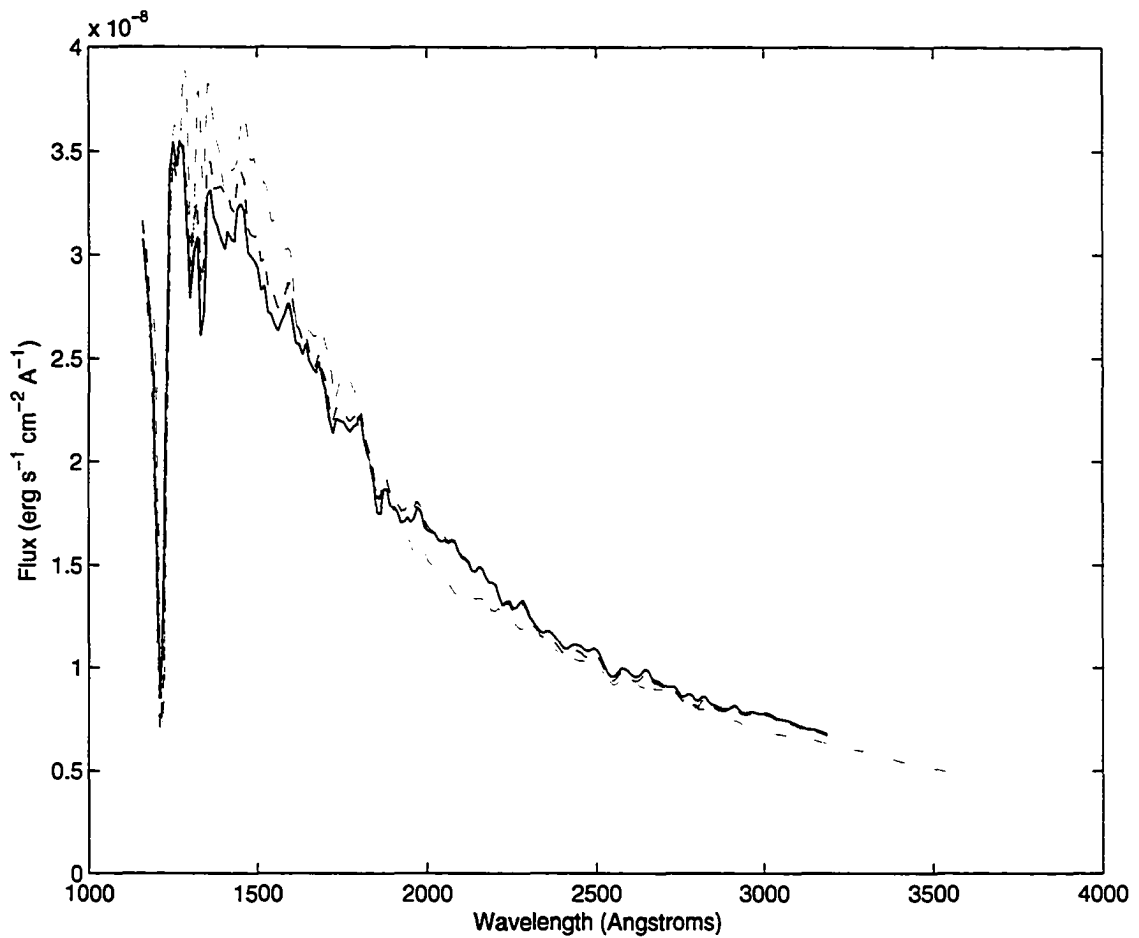


Figure 5.6: The SED for a  $6.5 M_{\odot}$  model (solid) inclined at  $80^{\circ}$  and a  $7 M_{\odot}$  model (dashed) inclined at  $84^{\circ}$ . Although the structure of the two models is very different, there is little visible expression of this in the SED. However, both models are very different from the observed SED of Achernar (dot-dashed), particularly in the peak of the spectrum around  $1500 \text{ \AA}$

and  $82^{\circ}$  respectively. However, I still failed to match the observed oblateness of  $a/b = 1.56$ , as both these models have ratios of  $a/b \sim 1.2$

Overall, there are only small differences between the SEDs produced by my two rotating models, despite different surface temperature distributions and underlying physical structure. This seems to indicate that my inability to produce structure models to match the oblateness observed by Domiciano de Souza *et al.* (2003) will have little effect on my ability to reproduce the spectra. It may be possible to exploit differences that exist in the individual lines of these spectra (Collins, 1974; Collins & Sonneborn, 1977), but this possibility is not explored in this thesis.

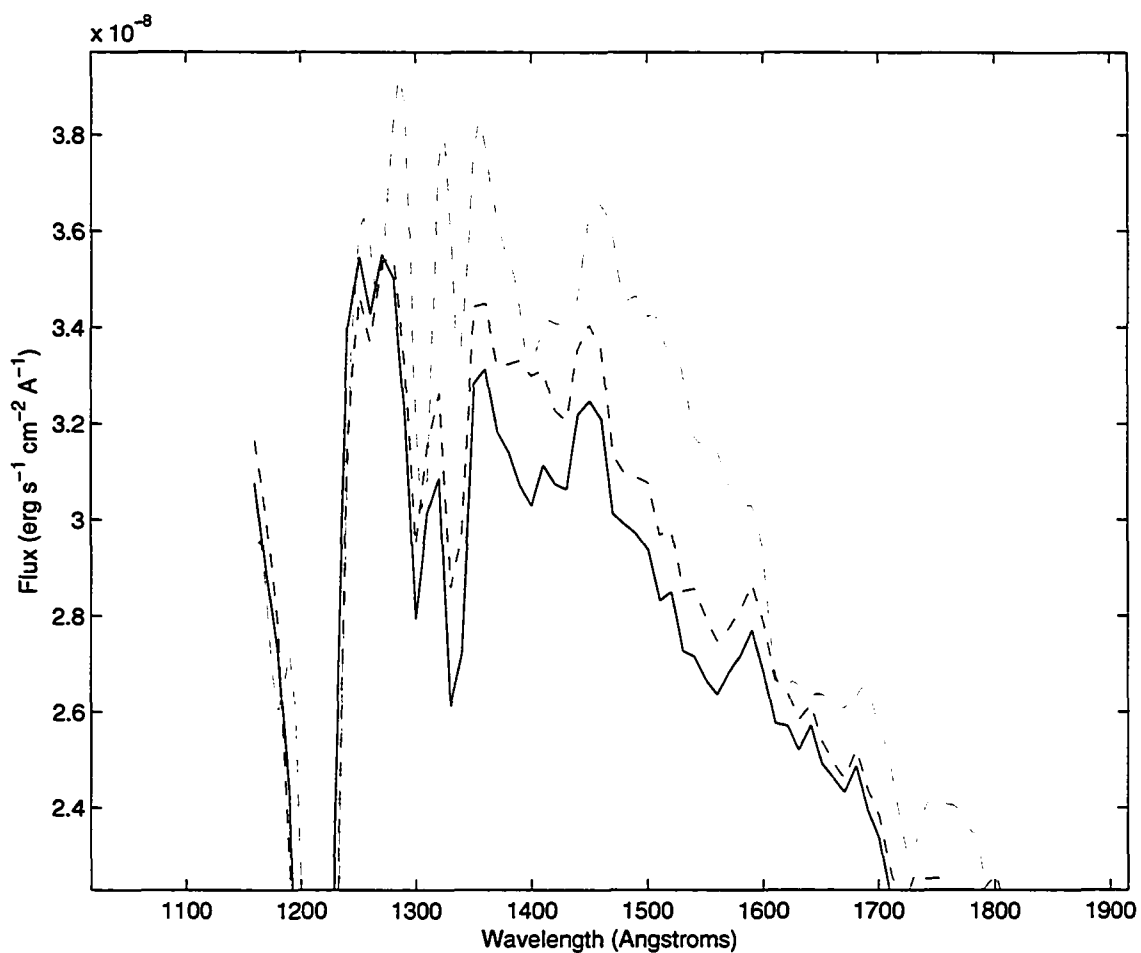


Figure 5.7: Same as for Fig. 5.6 but zoomed in to highlight the differences in the peak of the spectrum.

Table 5.1: Properties of models compared to the observed properties of Achernar

Model	$T_{eff}$ (K)	$L$ ( $L_{\odot}$ )	$v_{eq}$ ( $\text{km s}^{-1}$ )	Inclination	a/b (observed)
Achernar	14510	3311	225 <sup>1</sup>	unknown	1.56
6.5 $M_{\odot}$	14649	3377	223	82°	1.20
7.0 $M_{\odot}$	14492	3752	208	90°	1.17

<sup>1</sup> Observed  $v \sin i$  of Achernar.

Note: The observed oblateness of the models is given based on the angle of inclination required to match the observed  $v \sin i$  of Achernar.

---

# Chapter 6

## Conclusions

I have modelled the spectral energy distribution of a deformed star. While my models are rotationally deformed, in principle this method could be used on any type of deformed star, such as a companion in a close binary. Although this method is well known, I have updated it by applying the 2D stellar evolution code ROTORC to generate more realistic surface temperature distributions than previously possible. This allows me to directly calculate the surface temperature and effective gravity as functions of colatitude without resorting to approximations such as von Zeipel's law. This method is also valid over any spectral range and wavelength resolution, as long as the appropriate model atmospheres and intensity grids can be produced. I have re-sampled the intensity grid at 10 Å spacing for comparison with the OAO-2 data. At this resolution, the Doppler effects are insignificant. However, at higher resolution, Doppler effects would need to be included.

I find significant differences in the shapes of the observed SED as a function of the inclination of the rotation axis to the observer. These differences could mean that the effective temperature determined by an observer may have a complex relation to the physical temperature of the star as a whole. However, by comparing the SEDs resulting from two different stellar structure models, I have found that there is no obvious information on the oblateness of the star to be gleaned from the overall shape of the SED. If this method can be used to determine  $v$  and  $i$  separately, it will have to be done by studying individual spectral lines.

With my models, I have also attempted to reproduce as many of the observed properties of Achernar as possible, particularly the oblateness measurements of Domiciano de Souza *et al.* (2003) and the SED observed by the OAO-2 satellite (Code & Meade, 1979). Unfortunately, I was unable to reproduce the observed oblateness using my models. I found that a significant amount of angular

---

momentum must be concentrated in the core of the star to redistribute enough mass to affect the surface shape. I was unable to find a law that allowed me to do this while keeping the surface velocity below critical rotation. This matching has been successfully done by Jackson *et al.* (2004), but due to differences in my codes, I was unable to reproduce these models. At the present time, my code requires the maximum radius to be the equatorial radius. As the angular momentum increases and becomes more centrally concentrated, some models develop a bulge, with the maximum radius occurring at colatitudes of  $\sim 70\text{-}80^\circ$ . I believe this restricts my models and prevents them from becoming as oblate as those of Jackson *et al.* (2004). Despite this, based on the results of my synthetic SEDs described above, the shape of my underlying structure models is unlikely to have a significant effect on the synthetic spectra. Of the synthetic SEDs I have produced, the best matches are models inclined at  $80^\circ$  and  $84^\circ$ , corresponding to the  $6.5$  and  $7 M_\odot$  models, respectively. These inclinations also closely reproduce the observed  $v \sin i$  of Achernar, which requires  $i = 82^\circ$  and  $90^\circ$  respectively. However, the SED matches are poor, particularly near the peak of the spectra near  $1500 \text{ \AA}$ . The oblateness of the star does not appear to have a significant effect on the observed SED.

Despite the problems I have encountered with reproducing the observations, interferometric observations hold great promise. Combined with recent developments in asteroseismology, these techniques finally allow astronomers to begin to understand stellar rotation. As these observational techniques are developed, the results will become more accurate and more numerous, which will allow astronomers to develop better models. The first steps are being made towards an understanding of how stars rotate and what the effects of that rotation are, but there is still much work to be done.

---

# Bibliography

- Allen, C. W. 1973, *Astrophysical Quantities* (3d ed.; London: Athlone)
- Andrews, P.J., & Breger, M. 1966. *Observatory*, 86, 108
- Antia, H.M. & Basu, S. 2005. *ApJL*, 620, L129
- Asplund, M., Grevesse, N. & Sauval, A.J. 2005 in ASP conference series, in press, *Cosmic Abundances as Records of Stellar Evolution and Nucleosynthesis*, eds. F.N. Bash & T.G. Barnes.
- Bahcall, J.N., Serenelli, A.M. & Basu, S. 2005. *ApJL*, 621, L85
- Balona, L.A., Engelbrecht, C.A. & Marang, F. 1986. *MNRAS*, 227, 123
- Bautista, M. A., Romano, P., & Pradhan, A. K., 1998, *ApJS*, 118, 259
- Bodenheimer, P. 1971. *ApJ*, 167, 153
- Brown, P.J.F., Dufton, P.L., Lennon, D.J. & Keenan, F.P. 1986. *MNRAS*, 220, 1003
- Carroll, B.W. & Ostlie, D.A. 1996. *An Introduction to Modern Astrophysics*. Addison-Wesley, Don Mills, ON.
- Cassinelli, J.P. 1987. in *Physics of Be stars*, ed. A. Slettebak & T.P. Snow (Cambridge: Cambridge Univ. Press), 106
- Clement, M.J. 1974. *ApJ*, 194, 709
- Clement, M.J. 1978. *ApJ*, 222, 967
- Clement, M.J. 1979. *ApJ*, 230, 230

- 
- Code, A.D., & Meade, M.R. 1979. *ApJS*, 39, 195
- Code, A.D., Davis, J., Bless, R.C. & Hanbury Brown, R. 1976. *ApJ*, 203, 417
- Cohen, M., Walker, R. G., Carter, B., Hammersley, P., Kidger, M., & Noguchi, K. 1999, *AJ*, 117, 1864
- Collins, G.W. 1966. *ApJ*, 146, 914
- Collins, G.W. 1974. *ApJ*, 191, 157
- Collins, G.W. & Sonneborn, G.H. 1977. *ApJS*, 34, 41
- Collins, G.W. & Smith, R.C. 1985. *MNRAS*, 213, 519
- Collins, G.W. 1987, in *IAU Colloq. 92, Physics of Be Stars*, ed. A. Slettebak & T.P. Snow (Cambridge: Cambridge Univ. Press), 3
- Dachs, J., Eichendorf, W., Schleicher, H., Schmidt-Kaler, Th., Stift, M. & Tug, H. 1981. *A&AS*, 43, 427
- Dafon, S., Cunha, K., Butler, K. & Smith, V.V. 2001. *ApJ*, 563, 325
- Deupree, R.G. 1990. *ApJ*. 357, 175
- Deupree, R.G. 1995. *ApJ*, 439, 357
- Deupree, R.G. 1998. *ApJ*, 499, 340
- Deupree, R.G. 2000. *ApJ*, 543, 395
- Deupree, R.G. 2001. *ApJ*, 552, 268
- Domiciano de Souza, A., Kervella, P., Jankov, S., Abe, L., Vakili, F., di Folco, E., & Paresce, F. 2003. *A&A*, 407, L47
- Domiciano de Souza, A., Vakili, F., Jankov, S., Janot-Pacheco, E. & Abe, L. 2002. *A&A*, 393, 345

- 
- Drawin, H. W., 1961, *Z. Phys.*, 164, 513
- Faulkner, J, Roxburgh, I.W. & Strittmatter, P.A. 1968. *ApJ*, 151, 203
- Gehren, T., Nissen, P.E., Kudritzki, R.P. & Butler, K. 1985. in *Proc. ESO Workshop 21, Production and Distribution of C, N,O Elements*, ed. I.J. Danziger, F. Matteucci & K. Kjær (Garching: ESO), 171
- Gies, D.R. & Lambert, D.L. 1992. *ApJ*, 387, 673
- Hanbury Brown, R., Davis, J. & Allen, L.R. 1974. *MNRAS*, 167, 121
- Hardop, J. & Strittmatter, P.A. 1968. *ApJ*, 153, 465.
- Harmanec, P. 1988. *Bull. Astron. Inst. Czechoslovakia*, 39, 329
- Hauschildt, P.H. and Baron, E., 1999, *J. Comp. App. Math.*, 109, 41
- Henry, L.G., Forbes, J.E. & Gould, N.L. 1964. *ApJ*, 139, 306
- Hiltner, W.A., Garrison, R.F. & Schild, R.E. 1969. *ApJ*, 157, 313
- Hoffleit, D. 1982. *The Bright Star Catalogue*. Yale University Observatory, New Haven, CT.
- Iglesias, C.A. & Rogers, F.J. 1996, *ApJ*, 464, 943
- Jackson, S. 1970. *ApJ*. 161, 579
- Jackson, S., MacGregor, K.B. & Skumanich, A. 2004. *ApJ*, 606, 1196
- Jackson, S., MacGregor, K.B. & Skumanich, A. 2005. *ApJS*, 156, 245
- Jaschek, M., Hubert-Deplace, A.-M., Hubert, H. & Jaschek, C. 1980. *A&A Suppl. Ser.*, 42, 103
- Jerzykiewicz, M. & Molenda-Żakowicz, J. 2000. *AcA*, 50, 369
- Kostik, R.I., Shchukina, N.G. & Rutten, R.J. 1996. *A&A*, 305, 325

- 
- Kurucz R.L. 1994, CD-ROM No 22, Atomic Data for Fe and Ni (Cambridge: SAO)
- Kurucz, R. L., & Bell, B. 1995, CD-ROM 23, Atomic Line List (Cambridge: SAO)
- Lennon, D.J., Kudritzki, R.P., Becker, S.R., Eber, F., Butler, K. & Groth, H.G. 1990, in A.S.P. Conf. Ser., Vol. 7, Properties of Hot Luminous Stars, ed. C.D. Garmany (San Francisco: ASP), 315
- Linnell, A.P. & Hubeny, I. 1994. ApJ, 434, 738
- Lovekin, C.C., Deupree, R.G., & Short, C.I. 2005. Submitted to ApJ
- Maeder, A., & Meynet, G. 2000. ARA&A, 38, 143.
- Maeder, G. & Peytremann, E. 1970. A&A, 7, 120
- Mark, J. W-K. 1968. ApJ, 154, 627
- Mathisen, R. 1984, Photo Cross Sections for Stellar Atmosphere Calculations: Compilation of References and Data (Inst. Theor. Astrophys. Publ. Ser. 1; Oslo: Univ. Oslo)
- Mihalas, D. 1978, Stellar Atmospheres (2nd ed; New York: W.H. Freeman)
- Ostriker, J.P & Mark, J.W-K. 1968. ApJ, 151, 1075
- Perryman, M.A.C., Lindegren, L., Kovalevsky, J., et al, 1997. A&A, 323, L49
- Porri, A. & Stalio, R. 1988. A&AS, 75, 371
- Porter, J.M., & Rivinius, T. 2003. PASP, 115, 1153
- Reilman, R. F. & Manson, S. T., 1979, ApJS, 40, 815
- Richtmyer, R.D. & Morton, K.W. 1957, Difference Methods for Initial Value Problems (New York, Interscience)
- Roxburgh, I.W., Griffith, J.S. & Sweet, P.A. 1965. ZAp, 61, 203

- 
- Sackman, I-J. & Anand, S.P.S. 1969. *ApJ*, 155, 257
- Sackmann, I-J. & Anand, S.P.S. 1970. *ApJ*, 162, 105
- Seaton, M. J., Yan, Y., Mihalas, D., & Pradhan, A. K., 1994, *MNRAS*, 266, 805
- Secchi, A. 1867. *Astronomische Nachrichten*, 68, 63
- Short, C. I., Hauschildt, P. H., Baron, E., 1999, *ApJ*, 525, 375
- Slettebak, A. 1949. *ApJ*, 110, 498
- Slettebak, A. 1982. *ApJS*, 50, 55
- Sofia, U.J. & Meyer, D.M. 2001. *ApJ*, 554, L221
- Struve, O. 1931. *ApJ*, 73, 94
- Sweet, P.A. & Roy, A.E. 1953. *MNRAS*, 1113, 701
- Torres, C.A.O., da Silva, L., Quast, G.R., de la Reza, R. & Jilinski, E. 2000. *AJ*, 120, 1410
- Van Regemorter, H., 1962, *ApJ*, 136, 906
- Townsend, R.H.D, Owock, S.P. & Howarth, I.D. 2004. *MNRAS*, 350, 189
- von Zeipel, H. 1924. *MNRAS*, 84, 665
- Zahn, J.-P. 1992. *A&A*, 265, 115
- Zhang, P., Chen, P.S. & He, J.H. 2004. *NA*
- Zorec, J. & Briot, D. 1997. *A&A*, 318, 443